materials

MDPI

Article

Effect of Nb Content on Tribocorrosion Behavior of TiZrNbTa Refractory Multi-Principal Element Alloys in Sodium Chloride Solution

Zening Wang, Yi Zhang, Jinping Wu, Yu Yan * and Lijie Qiao

Beijing Advanced Innovation Center for Materials Genome Engineering, Corrosion and Protection Center, Institute for Advanced Materials and Technology, University of Science and Technology Beijing, Beijing 100083, China; wangzeningning@163.com (Z.W.)

* Correspondence: yanyu@ustb.edu.cn

Abstract

In this work, the effect of Nb content on the microstructure, passive film stability, and tribocorrosion behavior of TiZrNbTa refractory multi-principal element alloys (RMPEAs) was evaluated in 0.9 wt.% NaCl solution. Three designed alloys, $Ti_{45}Zr_{45}Nb_5Ta_5$, $Ti_{35}Zr_{35}Nb_{25}Ta_5$ and $Ti_{31.67}Zr_{31.67}Nb_{31.67}Ta_5$, were examined via electrochemical measurements, reciprocating sliding tests, X-ray photoelectron spectroscopy and surface/subsurface characterization. All alloys exhibited a single-phase body-centered cubic (BCC) solid solution. Increasing Nb refined dendritic grains but aggravated elemental segregation and reduced hardness from 320 ± 10 HV to 230 ± 10 HV. Reductions in corrosion and passive current densities demonstrated improved corrosion resistance and passive film stability. However, repassivation kinetics deteriorated because reduced Ti and Zr availability limited their preferential oxidation, which governed rapid passive film formation on fresh surfaces. Accordingly, higher Nb did not yield superior tribocorrosion resistance. The wear mechanism shifted from mild abrasive wear with continuous tribofilms toward severe ploughing, plastic deformation, delamination and microcracking. Under open-circuit potential (OCP) conditions, the average friction coefficient increased from 0.51 ± 0.05 to 0.78 ± 0.08, and the tribocorrosion rate rose from (3.75 ± 0.11) × 10^{-3} to (10.27 ± 0.30) × 10^{-3} $mm^3 \cdot N^{-1} \cdot m^{-1}$. Pure mechanical wear accounted for 70.72–79.11% of total material loss, and corrosion-accelerated wear dominated the synergistic component. The degraded performance at high Nb contents arose from the combined influence of decreased hardness, severe segregation, pit-triggered crack growth and suppressed surface work hardening. All of these factors amplified corrosion-accelerated wear. These findings revealed the dual function of Nb in TiZrNbTa RMPEAs. Nb stabilized the passive film while exacerbating tribocorrosion damage.

Keywords: multi-principal element alloys; tribocorrosion; wear–corrosion synergy; XPS

Check for updates

Academic Editors: Bernardo Monteiro and Marta Dias

Received: 17 October 2026
Revised: 1 November 2026
Accepted: 4 November 2026
Published: 6 November 2026

Copyright: © 2026 by the authors. Licensee MDPI, Basel, Switzerland. This article is an open access article distributed under the terms and conditions of the Creative Commons Attribution (CC BY) license.

1. Introduction

Multi-principal element alloys (MPEAs), also known as high-entropy alloys (HEAs), open up an entirely new alloy design space. Their high configurational entropy, severe lattice distortion, sluggish diffusion and cocktail effect endow the alloys with unique phase stability, together with mechanical and chemical properties that are generally superior to those of conventional dilute solid solutions. Senkov et al. [1,2] proposed refractory multi-principal element alloys (RMPEAs) with refractory elements (Mo, Nb, Ta, W, V, Hf,

Zr, Ti) as principal constituents. Featuring high melting points, excellent high-temperature strength retention and high hardness, RMPEAs serve as candidate materials for extreme service environments. Furthermore, the favorable biocompatibility [3] and strong oxygen affinity [4] of their constituent elements yield outstanding passivation performance, granting RMPEAs great application potential in biomedical implant materials.

In certain service environments, material surfaces are subjected to both environmental corrosion and friction. The interplay between these two effects accelerates material degradation and failure [5,6]. MPEAs exhibit a broad tunability in surface properties such as passivation and oxidation resistance, rendering them highly appealing for tribocorrosion applications [7]. However, current research on the tribocorrosion behavior of MPEAs remains limited. Most existing studies focus on the mechanisms under individual corrosion or wear conditions, while the material damage mechanism under their coupled interaction remains unclear. Yang et al. [8] investigated the damage behavior of CoCrFeNi-X (Ti, Mn, Mo, Al) HEA coatings under reciprocating friction in a 3.5 wt.% NaCl solution. They found that friction increases the corrosion rate within the worn area by 2–3 orders of magnitude. Although corrosion products can reduce the friction coefficient, localized damage induced by corrosion significantly increases the wear volume, and corrosion-triggered wear serves as the primary contributor to material loss. Diao et al. [9] investigated the tribocorrosion mechanisms of $CoCrFeNiTi_x$ alloys in simulated seawater. Obvious corrosion-promoted wear appears in low-Ti alloys. For high-Ti alloys, corrosion of the R phase (HCP structure similar to Ni_3Fe) induces delamination of the Laves phase and degrades tribocorrosion performance. The $Ti_{0.3}$ alloy achieves the optimal tribocorrosion resistance owing to the anodic protection provided by the R phase. Wang et al. [10] quantitatively characterized the corrosion wear synergistic behaviors of FeCrNiCo(I-0), FeCrNiCoAl(I-Al) and FeCrNiCoMo(I-Mo) HEAs in artificial seawater. Preferential Al dissolution in the I-Al alloy yields a low friction coefficient and high wear rate. Molybdate-containing wear debris fills FCC-phase corrosion pits and gives the I-Mo alloy the lowest wear rate. Wear dominates tribocorrosion damage and the rise in corrosion rate induced by wear is 100 times that of the wear rate increase triggered by corrosion. Zhang et al. [11] investigated the tribocorrosion behavior of $CoCrFeNiCu_{0.3}$ HEAs with different Cu distribution states in 3.5 wt.% NaCl solution. Homogeneous Cu distribution suppresses corrosive microcouples and promotes the formation of protective chromium oxide layers. It transforms the tribocorrosion mechanism from abrasive and corrosive wear to mild abrasive and oxidative wear and achieves optimal tribocorrosion resistance. Chen et al. [12] studied the repassivation behavior of $Al_{0.1}CrCoFeNi$ MPEAs during tribocorrosion. They found that selective oxidation of Cr, Co and Fe during repassivation leads to Ni enrichment on the alloy surface. The increased Ni content raises the electron work function and reduces surface reactivity. It further inhibits the repassivation process after the passive film is damaged by pitting or tribocorrosion. These studies indicate that most studies on the tribocorrosion behavior of MPEAs focus on 3d transition metal alloy systems represented by CoCrFeNi. Existing studies have shown that there is a significant coupling interaction between friction and corrosion in MPEAs. On one hand, the type and content of alloy elements regulate the competition and synergy between wear and corrosion by changing phase composition and microstructure. On the other hand, the passivation behavior of alloys including the stability of passive films and their repassivation ability after damage directly affects the evolution of tribocorrosion damage and material loss rate.

Current studies on RMPEAs mainly focus on their corrosion resistance and corrosion mechanisms. Research on their tribocorrosion behavior especially the coupled interaction between wear and corrosion remains scarce. Zeng et al. [13] studied the tribocorrosion behavior of $Ti_xNbCrMoAl$ RHEAs with varied Ti contents in molten aluminum and found

their better tribocorrosion resistance than conventional materials. This improvement arises from reduced alloy reactivity with molten aluminum and hard corrosion products, while material failure is controlled by synergistic corrosion wear interplay of matrix corrosion and wear triggered spalling of corrosion products. Ling et al. [14] fabricated TiNbCr RMPEAs and investigated the effect of Ti/Nb atomic ratio on their tribocorrosion behavior in molten aluminum. The alloy with 40 at.% Nb retains the BCC structure and forms a triple-synergistic interfacial armoring mechanism. $Ti_{48}Nb_{40}Cr_{12}$ exhibits much lower volume loss than TC4 and H13 steel under molten aluminum tribocorrosion. Xiao et al. [15] alloyed TiZrHfNb-based RMPEAs with Ta and Mo to enhance their corrosion and wear resistance via passivation film formation and hardness improvement. Their work reveals coupled electrochemical and mechanical interactions during tribocorrosion. Tribocorrosion degradation under anodic potential is marginally higher than at open- circuit potential (OCP), and the $TiZrHfNb_{1.83}Mo_{1.83}$ alloy achieves the optimal tribocorrosion performance. It can be seen that the composition and ratio of alloying elements exert a significant regulatory effect on the tribocorrosion behavior of RMPEAs. By altering the phase composition of alloys, and the characteristics of surface passivation or corrosion product films, the coupled mechanism of corrosion and wear can be effectively modified, which further determines the evolution law of tribocorrosion damage of alloys. In the TiZrNbTa system, Nb possesses a relatively high elastic modulus and melting point among the constituent elements. Adjusting Nb content can directly modulate the valence electron concentration, lattice distortion degree, solid solution strengthening level and the strength–plasticity balance of the BCC matrix [16,17]. On the other hand, variations in Nb content may also alter the composition and stability of surface oxide films, thereby affecting the wear behavior of alloys [18–20]. Nevertheless, systematic research linking Nb alloying extent to the tribocorrosion behavior of TiZrNbTa RMPEAs remains scarce to date, and the underlying damage mechanism as well as the tribocorrosion interaction are still unclear.

In this work, three TiZrNbTa RMPEAs with controlled Nb content ($Ti_{45}Zr_{45}Nb_5Ta_5$, $Ti_{35}Zr_{35}Nb_{25}Ta_5$ and $Ti_{31.67}Zr_{31.67}Nb_{31.67}Ta_5$) were fabricated via arc melting. The microstructure, phase composition, and hardness of the alloys were systematically characterized. Their tribocorrosion behavior was evaluated in NaCl solution and the synergistic effect of friction and corrosion was quantified to distinguish material loss caused by mechanical wear and electrochemical corrosion. By correlating Nb content with microstructure characteristics mechanical response surface film properties and damage morphology, the mechanism of Nb content affecting alloy tribocorrosion was clarified, which provides theoretical guidance for the design of RMPEAs.

2. Materials and Methods

2.1. Material Preparation

Commercial pure Ti, Nb, Ta and Zr metals (all with purity of 99.9 wt.%, Beijing General Research Institute for Nonferrous Metals, Beijing, China) were used as raw materials in this study. RMPEAs were fabricated via arc melting in a water-cooled copper crucible under an argon atmosphere. To ensure compositional homogeneity, the molten alloy was remelted five times, followed by casting into a copper mold to obtain alloy ingots with uniform compositions. In this work, compositional homogenization was achieved solely by multiple arc remelting, and no subsequent homogenization heat treatment was performed on the as-cast alloys. All characterization tests in this study were carried out on the above-mentioned as-cast alloy specimens. Each ingot was cut into square sheets of 15.00 ± 0.05 mm $\times$ 5.00 ± 0.05 mm $\times$ 1.00 ± 0.02 mm by wire electrical discharge machining. The specimen surfaces were sequentially ground using silicon carbide abrasive papers

with grit sizes of 1000, 2000, 3000 and 5000 (Yingkou Sanzheng New Technology Industry Co., Ltd., Yingkou, China).

2.2. Microstructure Characterization

The phase constitution of the alloys was determined by X-ray diffraction (XRD, D8 Advance, Bruker, Karlsruhe, Germany) using Cu-Kα radiation. XRD patterns were collected over a 2θ range at a scanning speed of $5^\circ \cdot \mathrm{min}^{-1}$. Specimens for microstructural observation were cut from the as-cast ingots, sequentially ground with silicon carbide abrasive papers up to 5000 grit, and then polished with 0.04 μm diamond suspension (Truer, Suzhou, China), followed by ultrasonic cleaning in ethanol and warm-air drying. Back-scattered electron (BSE) imaging and energy-dispersive X-ray spectroscopy (EDS) were performed on a Zeiss SUPRA 55 field-emission scanning electron microscope (FE-SEM, Carl Zeiss AG, Oberkochen, Germany) at an accelerating voltage of 15 kV and a working distance of approximately 10 mm. EDS elemental mapping was acquired at 15 kV with a pixel dwell time of 100 μs and a map resolution of 1024 × 768 pixels. For quantitative compositional analysis, five point spectra were acquired in each of the dendritic and interdendritic regions with an acquisition time of 60 s per spectrum, and the results were quantified using the built-in ZAF (atomic number, absorption and fluorescence) correction without external standards. The characterization of the initial as-cast microstructure was carried out independently of the worn-track characterization after subsequent tribocorrosion tests.

2.3. Microhardness Testing

Microhardness tests of all alloy specimens were performed using a high-precision digital Vickers hardness tester (HVS-1000Z, Shanghai Caikon Optical Instrument Co., Ltd., Shanghai, China, load accuracy ± 0.5%). A programmed automatic loading dwell and unloading sequence was adopted for the test. The experimental parameters were set as follows: an applied load of 0.01 kg (10 gf, approximately 98.07 mN), a loading rate of $50\ \mu\mathrm{m}\cdot\mathrm{s}^{-1}$, and a dwell time of 15 s, followed by a 2 s stabilization period after unloading to obtain high-quality indentation images. Ten measurements were carried out at randomly selected areas on the surface of each specimen, and the arithmetic mean and standard deviation were calculated for the results.

2.4. Electrochemical Measurements

Electrochemical tests were performed in a standard three-electrode electrolytic cell. A saturated calomel electrode (SCE, Model 232, Shanghai INESA Scientific Instrument Co., Ltd., Shanghai, China) was used as the reference electrode, and a platinum sheet served as the counter electrode (Wuhan Corrtest Instruments Corp., Ltd., Wuhan, China). All electrochemical measurements were conducted with an Ivium Vertex electrochemical workstation (Ivium Technologies B.V., Eindhoven, The Netherlands) in 0.9 wt.% NaCl solution (sodium chloride, Sinopharm Chemical Reagent Co., Ltd., Shanghai, China) at room temperature (25 ± 2 °C) under atmospheric pressure. Although 0.5 M NaCl is commonly used in static corrosion studies, 0.9 wt.% NaCl (approximately 0.154 M) was selected to approximate physiological saline and provide a relevant medium for tribocorrosion under reciprocating sliding. This choice is particularly relevant to biomedical implants and components operating in mild saline environments, rather than the more aggressive high-chloride conditions encountered in marine applications. After connecting copper wires (Aladdin, Shanghai, China), the specimens were encapsulated with epoxy resin, leaving only the working surface (15 mm × 5 mm, i.e., 75 mm^2) exposed. The edges and back side were fully coated with epoxy resin (Shanghai Meixin Resin Co., Ltd., Shanghai, China), and after curing the encapsulation was examined under an optical microscope to confirm that no metal was exposed, so that the exposed area was accurately controlled and used for current-density

normalization. The specimens were then ground, alcohol-degreased (anhydrous ethanol, Sinopharm Chemical Reagent Co., Ltd., Shanghai, China), cleaned and warm-air-dried. Before testing, the working electrode was immersed in the electrolyte for 120 ± 2 min to allow the system potential to become relatively stable. Potentiodynamic polarization tests were performed under conditions with and without sliding contact. The potential scanning range was from 0.30 V negative to the corrosion potential (E_{corr}) up to 3.0 V_{SCE}, and the scanning rate was 1.0 $mV \cdot s^{-1}$. Although the scan rate used here is higher than lower steady-state-oriented values such as 0.16 $mV \cdot s^{-1}$, it is not expected to introduce a significant bias in the present comparative analysis of these strongly passivating TiZrNbTa RMPEAs [21,22]. Nevertheless, an appropriate potential scan rate is important for minimizing distortion in Tafel-slope and corrosion current density (i_{corr}) analyses [21,22]. In addition, the OCP and cathodic polarization curves of all samples were monitored under conditions with and without sliding contact. For each alloy, electrochemical measurements were performed on three independently prepared specimens, and all electrochemical parameters are reported as the mean and standard deviation.

2.5. Tribocorrosion Tests and Characterization

Tribocorrosion tests were carried out on the samples under reciprocating sliding conditions in 0.9 wt.% NaCl solution (identical to that used in the electrochemical measurements) using a tribometer (UMT-2, CETR Inc., Campbell, CA, USA) equipped with a linear reciprocating drive module and a three-electrode electrochemical cell. This custom-modified tribometer with a liquid corrosion-cell module provides precise normal-load and sliding-motion control (1 mN load resolution, 0.1 μm displacement resolution). Further equipment details are available in the reference [23]. During testing, a closed-loop-controlled precision loading stage maintains normal load. A high-resolution load cell records friction force for real-time calculation of the friction coefficient. A displacement-controlled linear drive defines reciprocating stroke and sliding frequency. The counterbody ball sits perpendicularly to specimens on the friction sensor. Its integrated electrochemical cell links to an Ivium Vertex workstation to collect open-circuit potential, current density and COF throughout sliding tests. The counterbody was an alumina (Al_2O_3) ball with a diameter of 10.00 ± 0.05 mm. The cyclic sliding stroke was 30.00 ± 0.05 mm at a frequency of 1.0 Hz, corresponding to a sliding speed of 0.06 ± 0.0001 $m \cdot s^{-1}$. The applied normal load was 1.0 N, and the maximum Hertz contact pressures were 288.5 ± 2.0 MPa, 321.6 ± 2.2 MPa and 336.8 ± 2.3 MPa for $Ti_{45}Zr_{45}Nb_5Ta_5$, $Ti_{35}Zr_{35}Nb_{25}Ta_5$ and $Ti_{31.67}Zr_{31.67}Nb_{31.67}Ta_5$ alloys, respectively. Tribocorrosion measurements were performed at the OCP and a cathodic potential of −0.8 V_{SCE}, with a friction duration of 1000 ± 2 s for both conditions. The tribocorrosion tests at the cathodic potential were used to obtain the pure wear rate, namely the purely mechanical wear. The evolution of OCP, cathodic and anodic current densities as well as the corresponding coefficient of friction (COF) were recorded before, during and after sliding. Each tribocorrosion test was repeated on three independently prepared specimens for every alloy. The friction coefficients, wear rates and characteristic electrochemical quantities are reported as the mean and standard deviation. Ten Vickers microhardness measurements were performed at different regions of the wear track after the tribological test. In contrast to the initial microstructure characterization described in Section 2.2, SEM, EDS and a 3D profilometer (LEXT OLS5000, Olympus Corporation, Hachioji, Tokyo, Japan) were then employed to characterize the morphology, chemical composition and three-dimensional topography of the wear tracks after tribocorrosion tests.

2.6. Characterization of Passive Film Composition

X-ray photoelectron spectroscopy (XPS, PHI Quantera SXM, Physical Electronics, Chanhassen, MN, USA) was utilized to investigate the chemical composition of passive films generated on the alloy surfaces. A monochromatic Al-Kα X-ray source (h_v = 1486.6 eV) was adopted for excitation. During XPS characterization, the photoelectron take-off angle was maintained at 45°, and the analysis area was a 100 μm spot. Survey spectra were recorded across a binding energy interval of 1200 eV, with the pass energy set to 55.0 eV and a spectral resolution of 0.1 eV.

3. Results

3.1. Phase Composition and Microstructure

Figure 1 shows the XRD patterns of as-cast $Ti_{45}Zr_{45}Nb_5Ta_5$, $Ti_{35}Zr_{35}Nb_{25}Ta_5$ and $Ti_{31.67}Zr_{31.67}Nb_{31.67}Ta_5$ alloys. For each alloy, the XRD measurement was repeated three times at different positions on the specimen surface, and the patterns were essentially identical, confirming the reproducibility of the phase constitution. Careful indexing of diffraction peaks confirms that these peaks correspond to the (110), (200), (211), (220) and (310) crystal planes of the body-centered cubic (BCC) structure. The diffraction peaks lie close to, and at the low-angle side of, the reference peak positions of bcc β-Ti (JCPDS No. 44-1288) and bcc Nb (JCPDS No. 35-0789), which is consistent with previously reported TiZrNbTa RMPEAs in reference [24]. Quantitative analysis based on Gaussian peak fitting yields lattice parameters of a = 3.435 ± 0.005 Å, 3.431 ± 0.002 Å and 3.391 ± 0.004 Å for the three alloys, respectively. As the Nb content increases from 5 at.% to 31.67 at.%, all diffraction peaks shift toward higher Bragg angles, approaching the bcc Nb-rich reference position. Taking the (110) reflection as an example, its position moves from 36.96° to 37.42°, indicating a gradual reduction in the lattice parameter of TiZrNbTa RMPEAs. Such peak shift originates from lattice contraction, which is associated with the decreased content of Zr (with the largest atomic radius) and the increased proportion of smaller Nb atoms [25,26]. In addition, no extra diffraction peaks originating from intermetallic compounds or precipitated phases are detected in the XRD patterns of the three TiZrNbTa RMPEAs. All three alloys maintain a single-phase BCC solid solution without secondary phases, demonstrating high phase stability of the TiZrNbTa system within the compositional range investigated in this work.

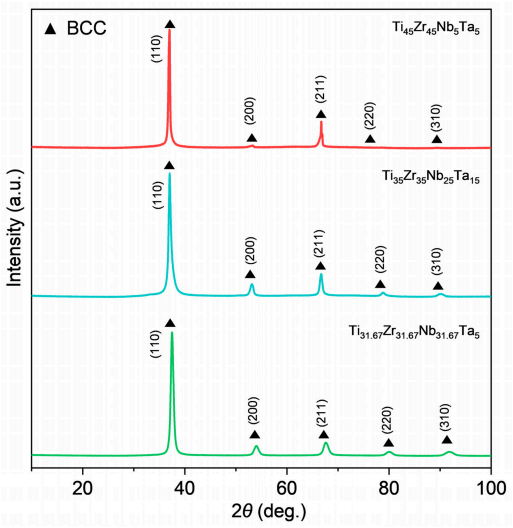

Figure 1. XRD patterns of all investigated samples.

The microstructures of as-cast $Ti_{45}Zr_{45}Nb_5Ta_5$, $Ti_{35}Zr_{35}Nb_{25}Ta_5$ and $Ti_{31.67}Zr_{31.67}Nb_{31.67}Ta_5$ alloys are shown in Figure 2a–c. All three alloys exhibit typical cast dendritic structures

with clear grain boundaries, and the grain size decreases with increasing Nb content. Here, the dendritic region (DR) refers to the primary dendrite arms and trunks that solidify first during cooling, whereas the interdendritic region (IDR) refers to the last-solidified areas located between neighboring dendrite arms. $Ti_{45}Zr_{45}Nb_5Ta_5$ shows regular herringbone dendrites, while $Ti_{35}Zr_{35}Nb_{25}Ta_5$ and $Ti_{31.67}Zr_{31.67}Nb_{31.67}Ta_5$ display dendritic morphology, and the dendritic arms are continuously refined as Nb content rises. This phenomenon originates from the low diffusion rate of Nb, which exerts a strong pinning effect on grain boundaries and restrains grain growth during solidification and cooling. The light-gray dendritic regions and dark-gray interdendritic regions in the back-scattered electron (BSE) images (as marked and distinguished in the BSE micrographs of Figure 2d–f) reflect solute redistribution during solidification. Nb and Ta possess higher atomic numbers than Ti and Zr, so the Nb/Ta-rich dendritic regions exhibit brighter contrast, while the Ti/Zr-rich interdendritic regions show darker contrast. Combined with EDS mapping quantitative results in Figure 2d–f and Table 1, the dendritic regions are enriched in Nb and Ta, whereas interdendritic regions possess higher concentrations of Ti and Zr [27]. All compositional values in Table 1 are reported as the mean together with its corresponding standard deviation. These data are derived from five EDS point analyses conducted at randomly selected positions within each region. The degree of elemental segregation increases significantly with rising Nb content. The composition of $Ti_{45}Zr_{45}Nb_5Ta_5$ is close to the TiZr quasi-binary system, which features similar atomic sizes, near-zero enthalpy of mixing and a partition coefficient close to unity for each element, leading to weak solute redistribution. As Nb content increases, high-melting-point Nb and Ta preferentially solidify into the solid phase, and Ti and Zr are rejected into the residual liquid and enriched in interdendritic areas [27,28]. The positive enthalpy of mixing and the large atomic size mismatch between Nb or Ta and Zr cause the solid phase to repel large-sized Zr atoms, thereby resulting in a partition coefficient of less than 1. Under non-equilibrium solidification, Zr continuously accumulates in the residual liquid and further intensifies interdendritic segregation [29]. Since Zr has a higher melting point than Ti, its interdendritic enrichment cannot be merely explained by melting point difference; it is mainly governed by thermodynamic and atomic size effects [29]. This indicates that increased Nb alloying is the primary cause for aggravated segregation. XRD results confirm that all three alloys maintain a single-phase BCC solid solution without intermetallic compounds or secondary phases. Within this compositional range, elemental segregation only induces local compositional fluctuation and lattice distortion in the solid solution, without altering the crystallographic symmetry of the matrix.

Table 1. EDS compositions (at.%) of the dendritic region (DR) and interdendritic region (IDRs) of the as-cast TiZrNbTa RMPEAs. DR and IDR denote the Nb/Ta-rich primary dendrite arms that solidified first and the Ti/Zr-rich regions between dendrite arms that solidified last, respectively.

Elements	Ti	Zr	Nb	Ta	Ti	Zr	Nb	Ta
	Dendritic				Interdendritic			
$Ti_{45}Zr_{45}Nb_5Ta_5$	44.59 ± 0.62	44.16 ± 0.58	5.54 ± 0.31	5.70 ± 0.28	45.11 ± 0.55	45.04 ± 0.61	5.05 ± 0.27	4.80 ± 0.24
$Ti_{35}Zr_{35}Nb_{25}Ta_5$	32.80 ± 0.71	29.44 ± 0.66	30.50 ± 0.72	7.26 ± 0.35	37.20 ± 0.68	39.30 ± 0.74	19.35 ± 0.58	3.15 ± 0.22
$Ti_{31.67}Zr_{31.67}Nb_{31.67}Ta_5$	29.47 ± 0.77	24.35 ± 0.69	38.40 ± 0.81	7.78 ± 0.38	35.10 ± 0.72	36.47 ± 0.78	24.90 ± 0.63	3.53 ± 0.25

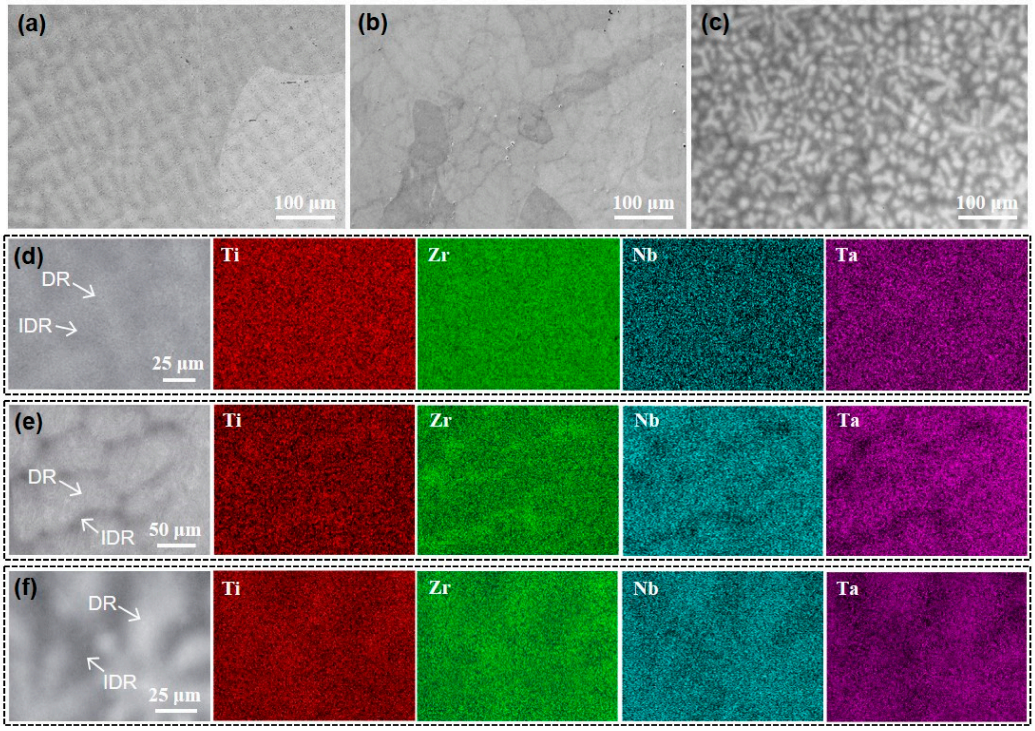

Figure 2. SEM-BSE images and corresponding EDS elemental mapping of as-cast TiZrNbTa RMPEAs: (**a**) $Ti_{45}Zr_{45}Nb_5Ta_5$; (**b**) $Ti_{35}Zr_{35}Nb_{25}Ta_5$; (**c**) $Ti_{31.67}Zr_{31.67}Nb_{31.67}Ta_5$; (**d**–**f**) EDS maps of Ti, Zr, Nb and Ta for alloys in (**a**–**c**), respectively.

3.2. Potentiodynamic Polarization

Figure 3 presents the potentiodynamic polarization (PDP) curves of all tested alloys under static and tribocorrosion conditions. All PDP curves pass directly from the Tafel region into a wide passive region, with no active dissolution peak observed, indicating that the alloys exhibit typical self-passivation behavior at the E_{corr} [30]. All electrochemical parameters were extracted from polarization curves using a unified procedure. The i_{corr} under both static and tribocorrosion conditions was acquired by fitting the cathodic Tafel line within the range of approximately 100 mV to 50 mV below the E_{corr} and extrapolating this line to E_{corr}. The anodic branch was excluded from fitting, as spontaneous passivation inhibits the formation of a Tafel region on the anodic side. This single-branch fitting method is a standard treatment for passivating metallic systems and has been validated through independent measurements on a wide range of passivating metallic systems [31–33]. For static tests, the i_{pass} was defined as the average current density over the potential window from 0 V_{SCE} to 1.0 V_{SCE}. Under tribocorrosion conditions, ipass was taken as the average current density over the potential window from −0.75 V_{SCE} to 0.5 V_{SCE}. The i_{pass} of the $Ti_{45}Zr_{45}Nb_5Ta_5$, $Ti_{35}Zr_{35}Nb_{25}Ta_5$, and $Ti_{31.67}Zr_{31.67}Nb_{31.67}Ta_5$ alloys are approximately 6.95 ± 0.83, 4.27 ± 0.78, and 3.93 ± 0.75 $\mu A \cdot cm^{-2}$, respectively. As the potential increases, a pronounced current rise emerges at approximately 1.25 V_{SCE}, which mainly originates from the oxygen evolution reaction (OER) triggered by electron transfer across the surface oxide film [34,35]. In contrast, the magnitude of this current rise decreases with increasing Nb content, indicating that the passive film possesses enhanced dielectric properties and can effectively block electron transfer. Additionally, this behavior is also associated with the increased activation energy and reduced diffusivity of oxygen vacancies within the passive film [36]. This current rise mainly originates from the OER, while the chlorine evolution reaction (CER) exerts only minor effects. In near-neutral NaCl solution, the O_2/H_2O equilibrium potential (~0.82 V_{SHE}) is far lower than the measured onset potential (1.49 V_{SHE}), and this difference reflects the high OER overpotential on the passive film.

Although the equilibrium potential of CER in a 0.154 M chloride medium (1.41 V_{SHE}) is only slightly lower than this onset potential, the kinetics of CER are substantially inhibited on valve-metal passive films (e.g., TiO_2 exhibits nearly no catalytic activity toward anodic chlorine evolution [37–40]). As the Nb content increases, the current amplitude gradually decreases. This trend is consistent with improved dielectric properties and reduced oxygen vacancy diffusivity of the passive film, demonstrating that the process is film-controlled and dominated by electron transport within the oxide layer. In contrast, CER depends on chloride activity and interfacial adsorption rather than the bulk properties of the passive film [38,39]. Admittedly, the contribution of minor chloride oxidation cannot be fully ruled out within the narrow potential window between the CER equilibrium potential and the onset potential. Furthermore, chemical and structural evolution of the passive film should also be considered. For instance, the growth of crystalline oxides inside the oxide film with increasing potential may accelerate the OER [41,42]. Further oxidation of constituent elements into higher-valence oxides may also slightly increase the anodic passive current density, yet such contributions remain limited. No obvious compositional-dependent differentiation of oxidation peak potentials is observed in this work, and the peak current does not rise with increasing Nb content.

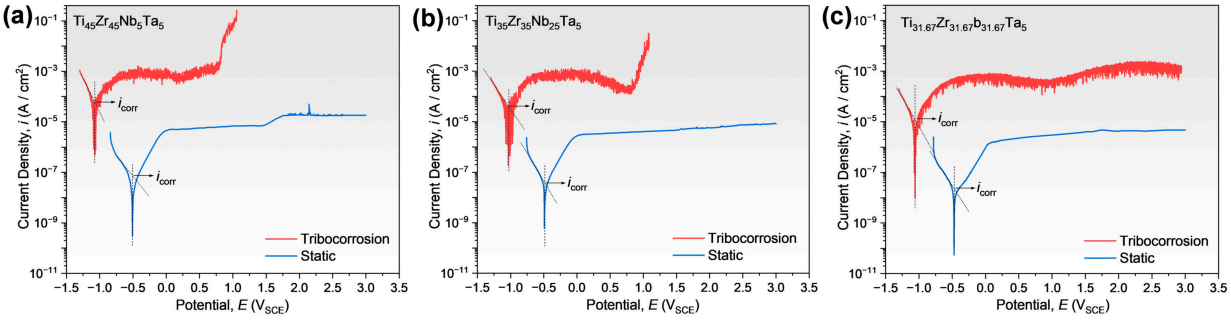

Figure 3. PDP curves of TiZrNbTa RMPEAs tested under static and tribocorrosion conditions: (**a**) $Ti_{45}Zr_{45}Nb_5Ta_5$; (**b**) $Ti_{35}Zr_{35}Nb_{25}Ta_5$; (**c**) $Ti_{31.67}Zr_{31.67}Nb_{31.67}Ta_5$.

The measured i_{corr} values are 76 ± 5, 40 ± 6, and 27 ± 3 nA·cm^{-2}, respectively, indicating that the dissolution rate of the passive film decreases with increasing Nb content. For the $Ti_{45}Zr_{45}Nb_5Ta_5$ and $Ti_{35}Zr_{35}Nb_{25}Ta_5$ alloys, obvious metastable pitting current peaks can be observed at approximately 2.0 V_{SCE}. These metastable events are distinguished from stable passive film breakdown by their transient character. The current spikes decay back to the passive current level within seconds as the metastable pits repassivate. Stable pitting breakdown is identified by an abrupt sustained current increase at least one order of magnitude above the passive level that does not decay upon continued polarization [43]. Notably, no stable film breakdown is detected within the scanned potential range up to 3.0 V_{SCE}. This result reveals the excellent stability of the passive films. Once friction is applied to the surface, the overall current density of the polarization curves increases, and the E_{corr} shifts markedly in the negative direction to approximately −1.0 V_{SCE} (Figure 3), with pronounced fluctuations in the overall current. This is attributed to the influence of stirring on the cathodic reaction at the electrode surface and the depassivation–repassivation process induced by friction [23,44]. Intense current oscillations in the anodic region arise from periodic depassivation–repassivation events synchronized with the reciprocating sliding cycle (1.0 Hz). Each sliding pass of the counterbody ruptures the passive film and triggers vigorous anodic dissolution. The current then gradually decays as the passive film reforms. The $Ti_{45}Zr_{45}Nb_5Ta_5$ alloy exhibits the largest oscillation amplitude, which decreases with rising Nb content. This confirms that such current fluctuations originate from the intrinsic competition between depassivation and repassivation of the material, instead of

instrumental noise. Friction leads to a significant increase in i_{corr}, rising to 57 ± 3, 26 ± 5, and 10 ± 5 μA·cm^{-2}, respectively, while the i_{pass} increases to 0.73 ± 0.05, 0.64 ± 0.08, and 0.46 ± 0.06 mA·cm^{-2}. Notably, for the $Ti_{45}Zr_{45}Nb_5Ta_5$ and $Ti_{35}Zr_{35}Nb_{25}Ta_5$ alloys under friction, the current continuously increases when the polarization potential reaches approximately 0.79 ± 0.07 V_{SCE} and 0.85 ± 0.05 V_{SCE}, respectively, implying localized accelerated dissolution or breakdown of the passive film. In contrast, when the polarization potential reaches 3.0 V_{SCE}, the passive current of the $Ti_{31.67}Zr_{31.67}Nb_{31.67}Ta_5$ alloy remains fluctuating within a relatively stable range, indicating that its passive film still possesses high protective capability under tribocorrosion conditions.

3.3. Open-Circuit Potential and Cathodic Polarization

Figure 4 presents the in situ electrochemical response of the OCP of the alloys to tribocorrosion. After approximately 2 h of immersion, OCP data were first acquired for about 900 s, and then mechanical friction was applied to the sample surface. Upon initiation of friction, the OCP drops sharply, indicating mechanical removal of the surface passive film [45]. The initial OCP values of $Ti_{45}Zr_{45}Nb_5Ta_5$, $Ti_{35}Zr_{35}Nb_{25}Ta_5$, and $Ti_{31.67}Zr_{31.67}Nb_{31.67}Ta_5$ alloys measured before friction are approximately −0.51 ± 0.02, −0.48 ± 0.02, and −0.46 ± 0.03 V_{SCE}, respectively. Friction renders the worn track anodic and the unfrictioned electrode area cathodic. Galvanic coupling between these two regions establishes a new electrode potential, which explains the OCP decrease under friction. The magnitude of the OCP reduction induced by friction for passive metals can be expressed as [46]:

$$E_c = E_s + a_c - b_c \log i_a - b_c \log \left[\left(\frac{LR}{A_c} \right) \left(\frac{k_{wt}}{0.003} \right)^{0.333} \right] \quad (1)$$

where E_c is the electrode potential after friction, i.e., the measured OCP value upon tribological loading. i_a denotes the anodic dissolution current density within the worn track. E_s is the measured OCP value before friction. a_c and b_c represent the anodic and cathodic Tafel slopes derived from static polarization curves, respectively. L and R are the worn track length and the radius of the counter ball, respectively. k_{wt} is the material wear rate, and A_c corresponds to the cathode area. Therefore, the primary factors affecting the OCP drop of the material are the dissolution current in the anodic region, the cathode area, and the mechanical wear rate of the material. Subsequent analysis reveals that the mechanical wear rate of the materials follows the order: $Ti_{31.67}Zr_{31.67}Nb_{31.67}Ta_5$ > $Ti_{35}Zr_{35}Nb_{25}Ta_5$ > $Ti_{45}Zr_{45}Nb_5Ta_5$, while the cathode area exhibits the opposite trend. Nevertheless, the OCP reductions are 0.55 ± 0.07, 0.54 ± 0.05, and 0.52 ± 0.05 V, respectively. According to the above equation, this indicates that the anodic dissolution current generated on the fresh alloy surface during friction decreases in the sequence $Ti_{45}Zr_{45}Nb_5Ta_5$ > $Ti_{35}Zr_{35}Nb_{25}Ta_5$ > $Ti_{31.67}Zr_{31.67}Nb_{31.67}Ta_5$. This trend is consistent with the order of i_{corr} obtained from PDP tests under friction, meaning that the cation dissolution rate of the fresh alloy surface is suppressed with increasing Nb content. During friction, depassivation and repassivation processes on the material surface exist in dynamic equilibrium, causing the OCP to fluctuate around a certain potential level. The $Ti_{45}Zr_{45}Nb_5Ta_5$ alloy delivers the maximum OCP fluctuation amplitude. This amplitude decreases for the $Ti_{35}Zr_{35}Nb_{25}Ta_5$ alloy. The $Ti_{31.67}Zr_{31.67}Nb_{31.67}Ta_5$ alloy exhibits the weakest OCP fluctuation. The more pronounced OCP fluctuations reflect a stronger dynamic competition between friction-induced depassivation and surface repassivation, which is consistent with the rapid repassivation behavior of the Ti- and Zr-rich alloy. It therefore demonstrates that increasing the contents of Ti and Zr in the alloy is beneficial to its repassivation performance. It should be noted that each tribocorrosion test was repeated three times under identical conditions, and the results were highly reproducible.

The characteristic quantities derived from Figure 4, including the OCP at the onset of friction, the magnitude of the friction-induced OCP drop, the OCP fluctuation amplitude, showed small scatter among the three parallel runs, confirming the reliability of the in situ electrochemical and friction data. When friction ceases, repassivation occurs and the OCP gradually recovers to a value close to its initial level. The rate of OCP rise during passivation recovery differs among the three alloys. Within a specified time period after the onset of repassivation, the repassivation rate can be quantitatively analyzed using the following formula [47]:

$$\Delta E = k_1 \log t + k_2 \quad (2)$$

where ΔE is the amplitude of potential rise, t is the passivation recovery time, k_1 is the repassivation rate, and k_2 is a constant related to the solution. The value of k_2 is 0.1 for NaCl solution [47]. According to Equation (2), the linear region of OCP versus log t after the cessation of friction was fitted, yielding k_1 of 0.176 ± 0.011, 0.152 ± 0.015 and 0.129 ± 0.009 for the $Ti_{45}Zr_{45}Nb_5Ta_5$, $Ti_{35}Zr_{35}Nb_{25}Ta_5$, and $Ti_{31.67}Zr_{31.67}Nb_{31.67}Ta_5$ alloys, respectively. This indicates that a high cation dissolution rate on the bare metal surface facilitates the nucleation and growth of the passive film.

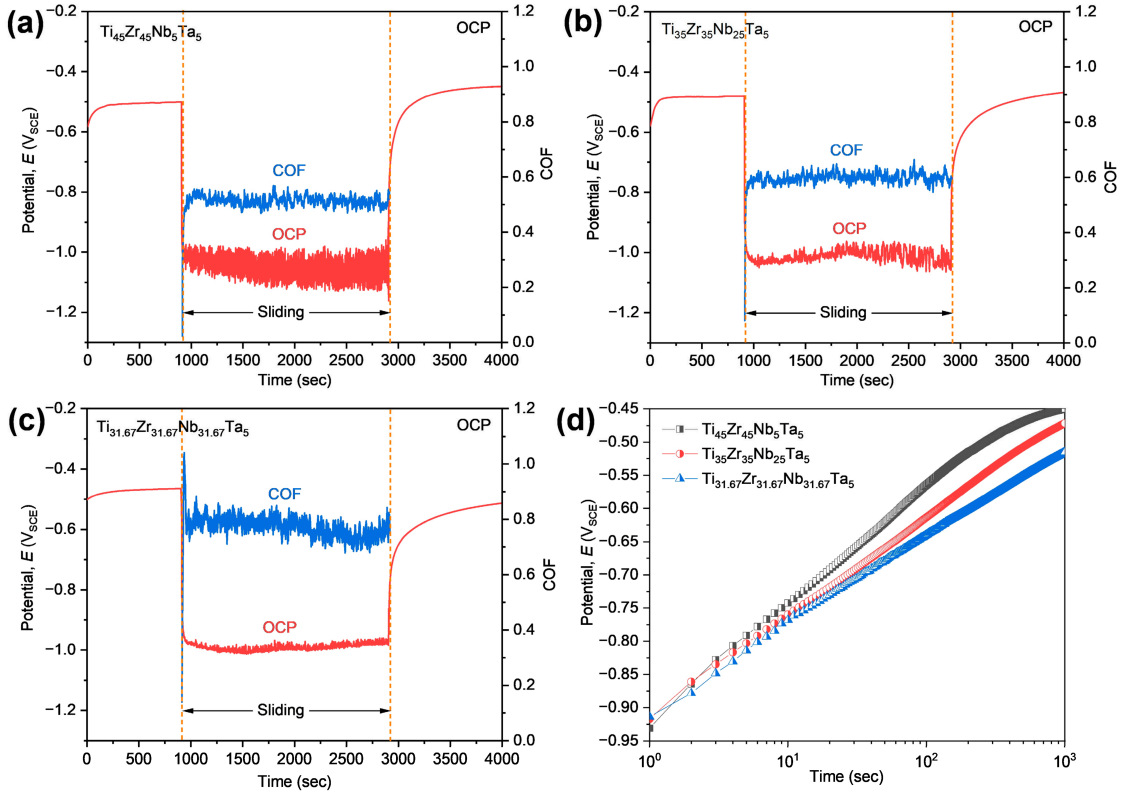

Figure 4. OCP and friction coefficient evolution of TiZrNbTa RMPEAs during tribocorrosion sliding: (**a**) $Ti_{45}Zr_{45}Nb_5Ta_5$; (**b**) $Ti_{35}Zr_{35}Nb_{25}Ta_5$; (**c**) $Ti_{31.67}Zr_{31.67}Nb_{31.67}Ta_5$; (**d**) OCP recovery curves after sliding in logarithmic time scale.

The friction coefficients of the three alloys monitored during friction at the OCP potential are shown in Figure 4a–c. It can be seen that the friction coefficients of the three alloys remain stable during sliding. The average friction coefficients of $Ti_{45}Zr_{45}Nb_5Ta_5$, $Ti_{35}Zr_{35}Nb_{25}Ta_5$, and $Ti_{31.67}Zr_{31.67}Nb_{31.67}Ta_5$ alloys are 0.51 ± 0.05, 0.60 ± 0.04 and 0.78 ± 0.08, respectively. Under identical experimental conditions, the friction coefficient of metallic materials is mainly affected by surface roughness, surface lubrication and surface hardness. Owing to the identical surface treatment and passivated state of the specimens, the influence of surface roughness can be neglected. Therefore, the friction coefficient is

primarily determined by the stability of the tribofilms formed on the tribocorrosion surfaces of the three alloys and by the tribocorrosion mechanism [48,49]. The tribocorrosion mechanisms of all tested alloys are discussed in the following section to analyze their effects on the friction coefficient. Under the applied cathodic potential condition, friction leads to an increase in cathodic current density for the three alloys (Figure 5a–c). This is attributed to the stirring effect of friction, which accelerates the cathodic reaction kinetics on the electrode surface. Furthermore, friction removes the residual passive film on the surface and exposes fresh metal, resulting in further acceleration of the cathodic reaction within the wear track region [49]. The residual current fluctuations under cathodic polarization (Figure 5) do not arise from anodic dissolution, which is suppressed at -0.8 V_{SCE}, but mainly reflect the intermittent exposure of fresh metal areas and the entrainment and ejection of oxide debris (third-body effects) synchronized with the sliding cycles, as well as the perturbation of mass transfer in the cathodic reaction at the electrode surface caused by mechanical stirring. At cathodic potential, the average friction coefficients of $Ti_{45}Zr_{45}Nb_5Ta_5$, $Ti_{35}Zr_{35}Nb_{25}Ta_5$, and $Ti_{31.67}Zr_{31.67}Nb_{31.67}Ta_5$ alloys are 0.54 ± 0.05, 0.67 ± 0.05 and 0.89 ± 0.09, respectively. The cathodic potential suppresses both the anodic dissolution of the metal and oxide film formation, which may to some extent inhibit tribofilm formation and thus lead to a higher friction coefficient than that under OCP conditions.

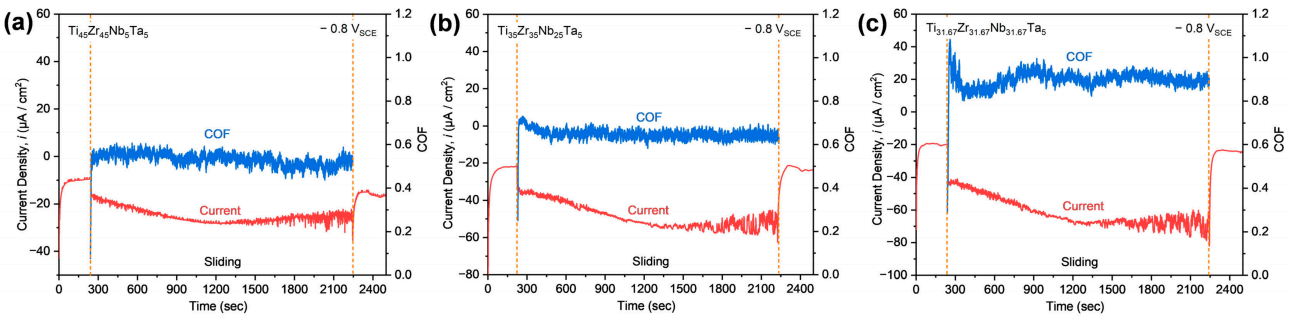

Figure 5. Current density and friction coefficient evolution of TiZrNbTa RMPEAs during tribocorrosion sliding at an applied cathodic potential of -0.8 V_{SCE}: (**a**) $Ti_{45}Zr_{45}Nb_5Ta_5$; (**b**) $Ti_{35}Zr_{35}Nb_{25}Ta_5$; (**c**) $Ti_{31.67}Zr_{31.67}Nb_{31.67}Ta_5$.

3.4. Characterization of Tribocorroded Surface Morphology

Figure 6 presents the SEM morphologies and corresponding back-scattered electron (BSE) images of tribocorrosion surfaces for the investigated alloys under OCP conditions. Abrasive wear features along the sliding direction can be observed on the tribocorrosion surface of the $Ti_{45}Zr_{45}Nb_5Ta_5$ alloy, which originate from micro-cutting induced by detached oxide particles (Figure 6a). Numerous island-like tribofilms are visible in the dark regions of its BSE image. The tribofilms are composed of oxides of each constituent element and contain a small amount of Al. The Al signal originates from minor material transfer caused by wear of the friction counterpart. The $Ti_{35}Zr_{35}Nb_{25}Ta_5$ alloy exhibits aggravated abrasive wear with abundant residual oxide particles on the surface. BSE and EDS results confirm that more discontinuous tribofilms form on the tribocorrosion surface (Figure 6b). Wider ploughing grooves and deteriorated abrasive wear appear on the tribocorrosion surface of the $Ti_{31.67}Zr_{31.67}Nb_{31.67}Ta_5$ alloy. Obvious material delamination, plastic deformation and microcrack propagation are also identified, and tiny pits are observed in local regions (Figure 6c). This phenomenon arises from friction-induced removal of the passive film, which accelerates chloride attack on the freshly exposed substrate surface. The coverage area and continuity of tribofilms on this alloy decrease. EDS measurements reveal a higher Al content in the tribofilms. This is attributed to severe wear of the friction counterpart and substantial transfer of counterpart materials onto the sample surface.

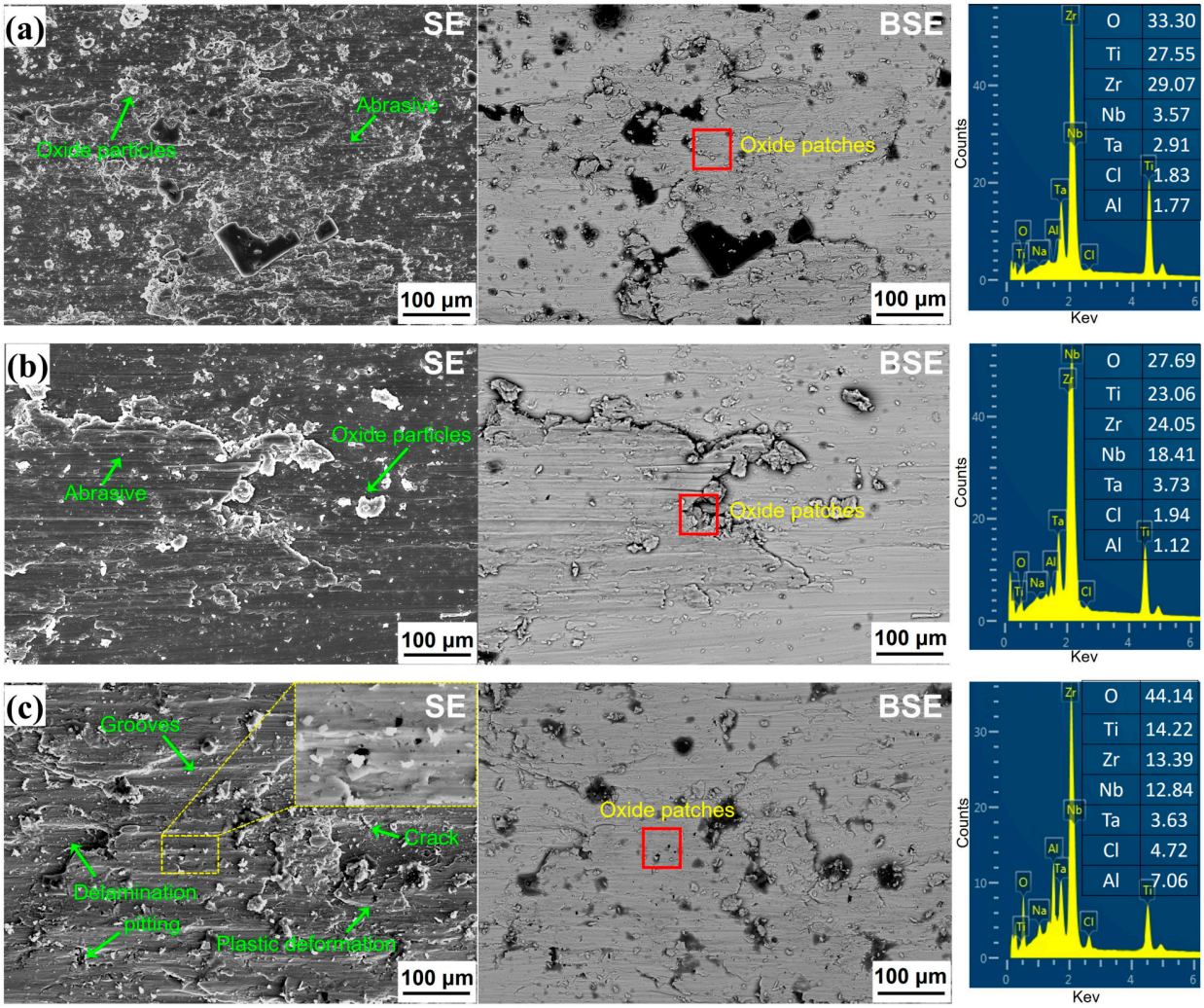

Figure 6. SEM, BSE, together with EDS spectra of tribocorrosion wear tracks on TiZrNbTa RMPEAs under OCP condition: (**a**) $Ti_{45}Zr_{45}Nb_5Ta_5$; (**b**) $Ti_{35}Zr_{35}Nb_{25}Ta_5$; (**c**) $Ti_{31.67}Zr_{31.67}Nb_{31.67}Ta_5$.

When the cathodic potential is applied, the degree of abrasive wear on the tribocorrosion surfaces of $Ti_{45}Zr_{45}Nb_5Ta_5$ and $Ti_{35}Zr_{35}Nb_{25}Ta_5$ alloys exhibits no significant change. Obvious plastic deformation features emerge in local regions of the specimens. The continuity of the tribofilm decreases and local cracking and spalling can be observed, as shown in Figure 7a,b. The plastic deformation and delamination wear on the tribocorrosion surface of $Ti_{31.67}Zr_{31.67}Nb_{31.67}Ta_5$ alloy are further intensified, and prominent spalling of the tribofilm occurs. EDS analyses reveal a reduced Cl content on the tribocorrosion surface. This indicates that cathodic polarization suppresses chloride-induced surface corrosion. The above results demonstrate that cathodic potential aggravates surface wear damage for all tested alloys. The tribocorrosion surface morphologies confirm that the wear severity follows the order $Ti_{31.67}Zr_{31.67}Nb_{31.67}Ta_5$ > $Ti_{35}Zr_{35}Nb_{25}Ta_5$ > $Ti_{45}Zr_{45}Nb_5Ta_5$. It can therefore be concluded that increasing Nb content in TiZrNbTa alloys reduces their tribocorrosion resistance, and higher Nb content impairs the ability of the alloy to resist abrasive wear and delamination wear.

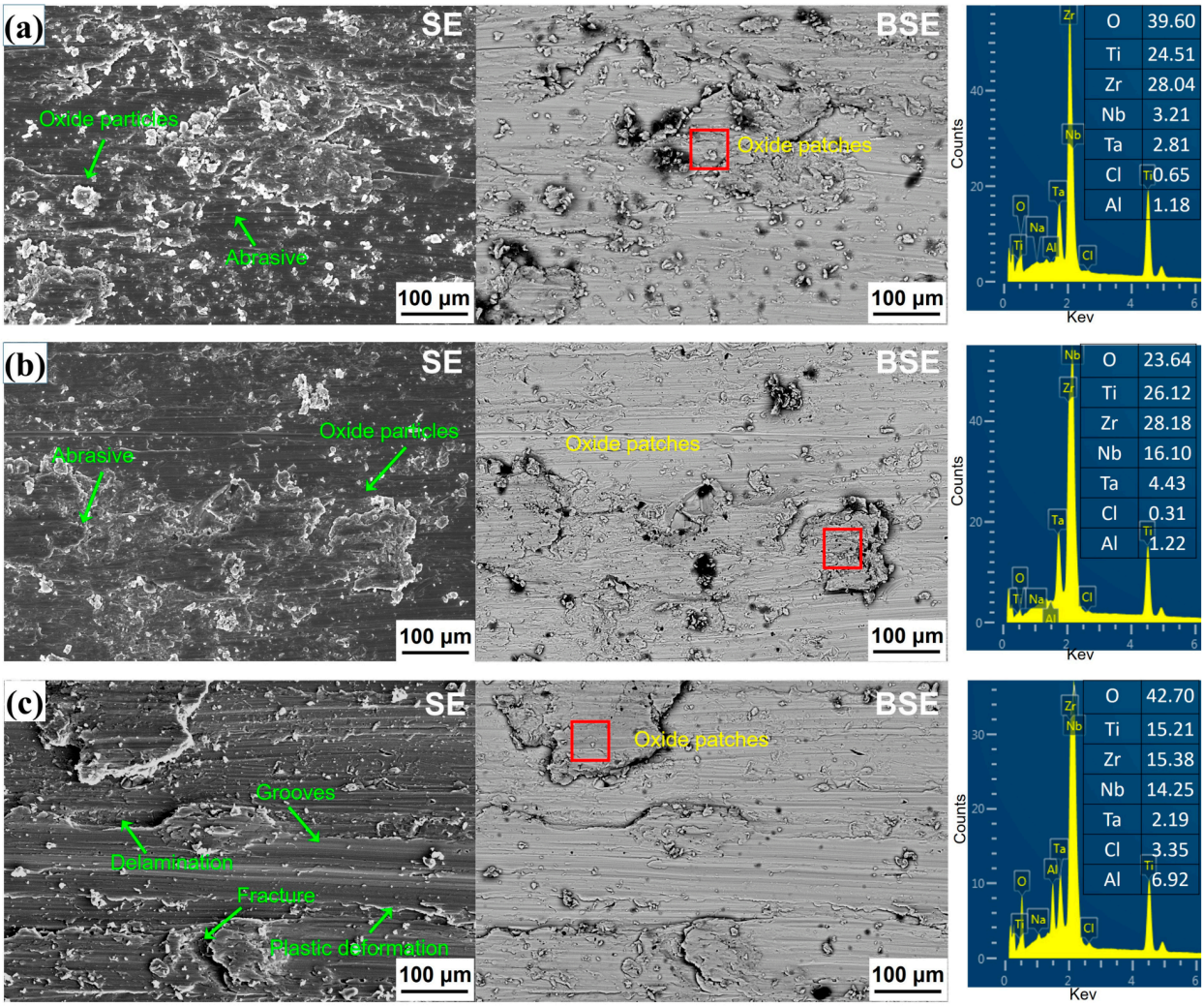

Figure 7. SEM, BSE, together with EDS spectra of tribocorrosion wear tracks on TiZrNbTa RMPEAs under −0.8 V_{SCE} cathodic potential: (**a**) $Ti_{45}Zr_{45}Nb_5Ta_5$; (**b**) $Ti_{35}Zr_{35}Nb_{25}Ta_5$; (**c**) $Ti_{31.67}Zr_{31.67}Nb_{31.67}Ta_5$.

3.5. Analysis of the Tribocorrosion Rate

Figure 8 presents the three-dimensional morphologies and cross-sectional profiles of wear tracks measured for the three alloys under OCP and applied cathodic potential conditions. Under both open-circuit and cathodic potentials, the depth and width of wear tracks increase with rising Nb content in the alloys. $Ti_{31.67}Zr_{31.67}Nb_{31.67}Ta_5$ exhibits markedly severer wear than the other two alloys, which is associated with severe ploughing and delamination wear. The trend indicates that increasing Nb fraction weakens the protective capacity of the mechanically mixed layer formed within the wear track during sliding. A higher Nb content slows the repassivation kinetics after film rupture, which extends the duration of active dissolution and facilitates the initiation and propagation of surface cracks that drive delamination. According to the Archard equation, the total tribocorrosion rate can be expressed as [50]:

$$k_{wt} = \frac{\Delta V}{L \times N} \tag{3}$$

where k_{wt} is the total tribocorrosion rate, ΔV is the total wear volume (mm^3), L is the sliding distance (m), and N is the normal load (N). The calculated tribocorrosion rates of $Ti_{45}Zr_{45}Nb_5Ta_5$, $Ti_{35}Zr_{35}Nb_{25}Ta_5$ and $Ti_{31.67}Zr_{31.67}Nb_{31.67}Ta_5$ alloys under open-circuit conditions are (3.75 ± 0.11) × 10^{-3}, (5.77 ± 0.17) × 10^{-3} and (10.27 ± 0.30) × 10^{-3}

$mm^3 \cdot N^{-1} \cdot m^{-1}$, respectively. Under cathodic potential, the values are $(2.97 \pm 0.09) \times 10^{-3}$, $(4.23 \pm 0.13) \times 10^{-3}$ and $(7.26 \pm 0.22) \times 10^{-3}$ $mm^3 \cdot N^{-1} \cdot m^{-1}$, respectively. For all three compositions, the cathodic condition yields a lower wear rate than OCP, which further verifies the coupling effect between mechanical damage and electrochemical corrosion in tribocorrosion. At -0.8 V_{SCE}, anodic dissolution is largely inhibited and the contribution of corrosion-accelerated wear is eliminated. The reduced tribocorrosion rate under cathodic potential is attributed to the corrosion suppression by cathodic polarization, where only pure mechanical wear dominates.

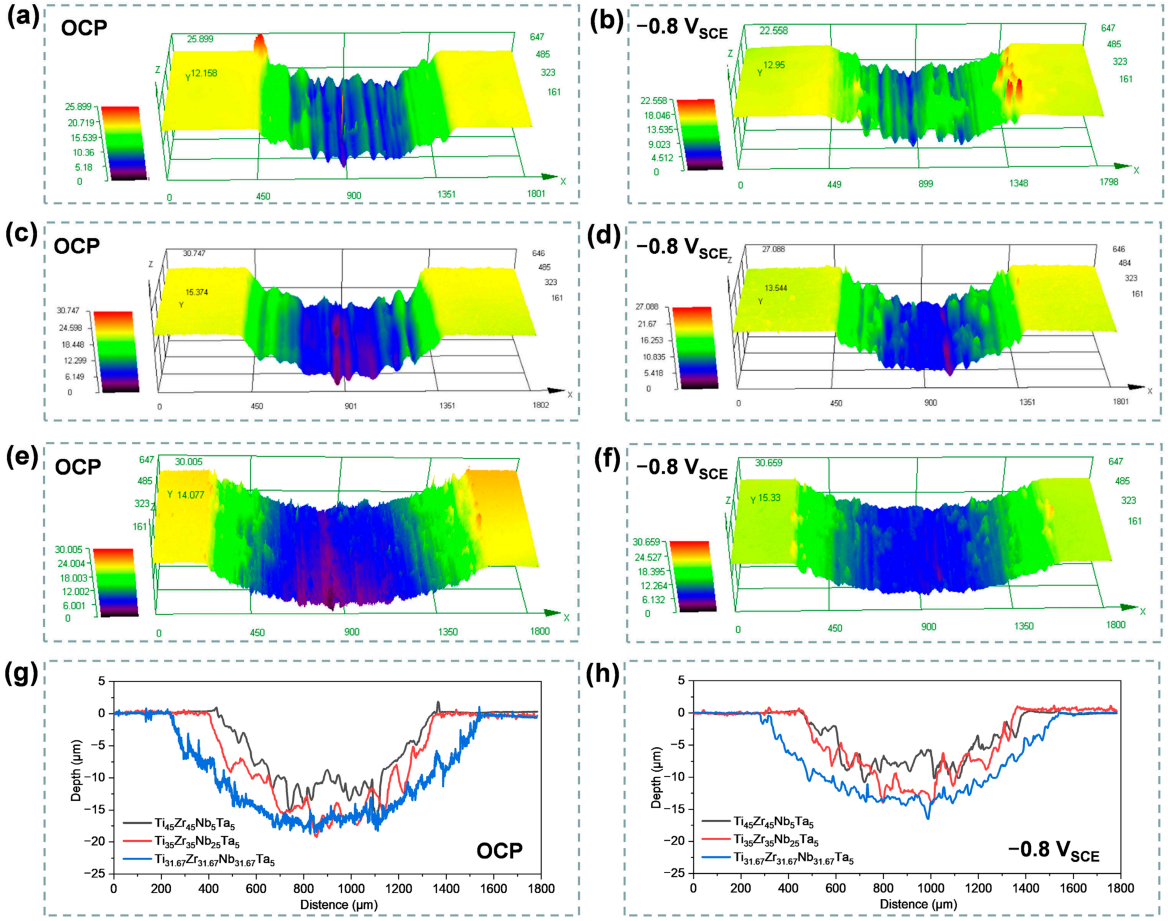

Figure 8. Three-dimensional topographies of wear tracks and corresponding cross-sectional profiles for TiZrNbTa RMPEAs under OCP and -0.8 V_{SCE} cathodic potential: (**a**,**b**) $Ti_{45}Zr_{45}Nb_5Ta_5$; (**c**,**d**) $Ti_{35}Zr_{35}Nb_{25}Ta_5$; (**e**,**f**) $Ti_{31.67}Zr_{31.67}Nb_{31.67}Ta_5$; (**g**) cross-sectional profiles under OCP; (**h**) cross-sectional profiles under -0.8 V_{SCE}.

3.6. XPS Characterization of Tribocorroded Surfaces

Figures 9 and 10 show the high-resolution XPS spectra of surface films on three alloys after tribocorrosion under OCP, followed by immersion in the solution for 10 s and 2 h, respectively. As shown in Figure 9, Ti and Zr preferentially form high-valence oxides at the initial stage of repassivation. In the high-resolution Ti 2p spectrum, the spin–orbit split doublet of Ti^{4+} dominates, with only weak signals of Ti^{3+}, Ti^{2+} and metallic Ti^0 detected on the low-binding-energy side. Similarly, the Zr 3d spectrum is dominated by the Zr^{4+} doublet, accompanied by minor Zr^{2+} and Zr^0 species. These results confirm that Ti and Zr can be rapidly oxidized to thermodynamically stable TiO_2 and ZrO_2 at the early nucleation stage of the passive film. Among the three alloy systems, the relative content of TiO_2 and ZrO_2 is the highest on the $Ti_{45}Zr_{45}Nb_5Ta_5$ surface. With the increase in Nb fraction and the corresponding reduction in Ti/Zr content in the alloy, the proportion

of intermediate-valence and metallic species of Ti and Zr rises, indicating insufficient oxidation. The Nb 3d spectrum is dominated by Nb^{5+} peaks, and the Ta 4f spectrum is dominated by Ta^{5+} peaks. Nevertheless, the relative intensities of the intermediate-valence and metallic characteristic peaks of Nb and Ta are markedly higher than those of Ti and Zr, indicating the slower oxidation rate and retarded growth of the passive film for Nb and Ta. Further comparison among the three alloys reveals that the relative fraction of Nb^{5+} increases and the peak intensities of intermediate-valence and metallic Nb species decrease with increasing Nb content, while no obvious changes are observed in the characteristic peaks of Ta at different valence states. The intensity of metallic peaks measured by XPS can qualitatively characterize the equivalent oxide film thickness and surface coverage of each element. A stronger metallic signal indicates a thinner corresponding oxide layer or poorer coverage integrity. The metallic signals of Ti and Zr are nearly undetectable, whereas relatively strong metallic signals remain for Nb and Ta. This result demonstrates that Ti and Zr undergo preferential oxidation at the initial repassivation stage and govern the rapid nucleation and growth of the oxide layer after the breakdown of the original passive film. Alloys with higher Ti and Zr contents possess faster repassivation rates on the fresh bare metallic surface, which is consistent with the violent fluctuation of potential curves during tribocorrosion under OCP conditions and the rapid potential recovery after tribocorrosion ceases.

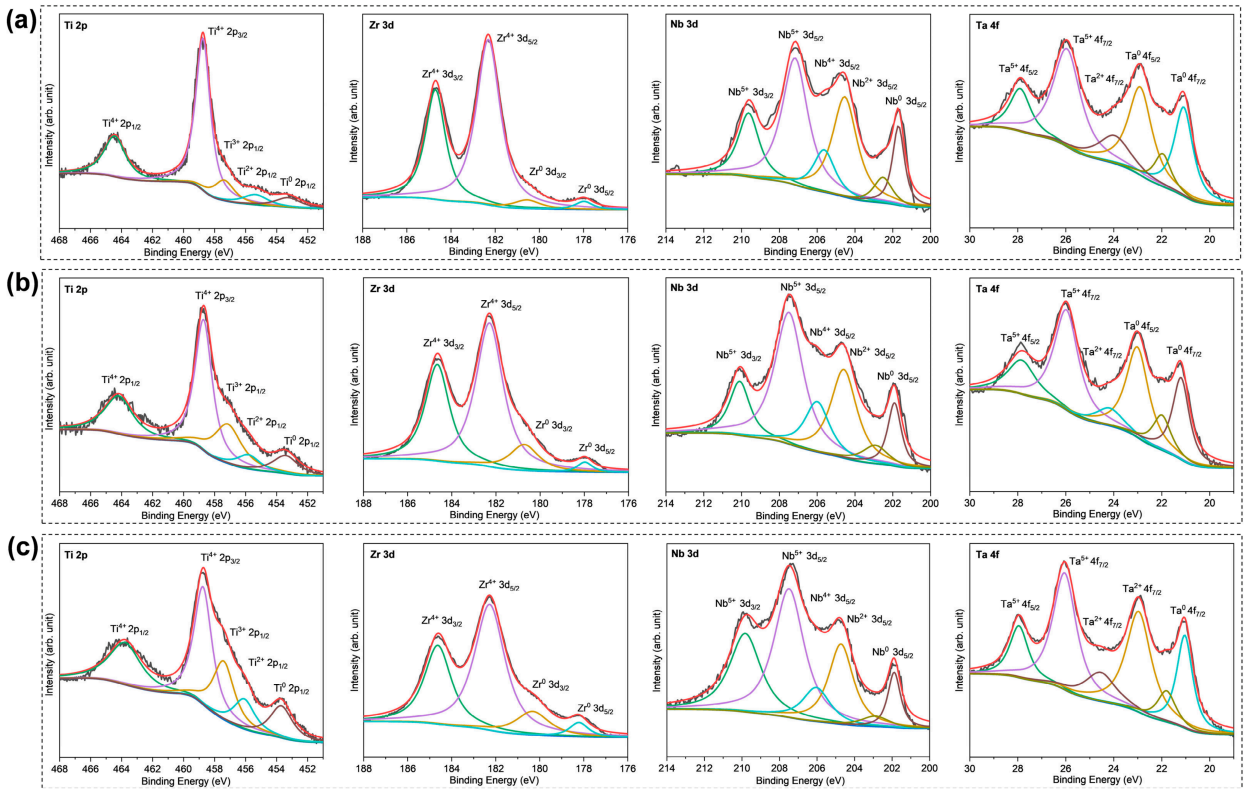

Figure 9. High-resolution XPS spectra (Ti 2p, Zr 3d, Nb 3d and Ta 4f) of the tribocorroded surfaces on TiZrNbTa RMPEAs after 10 s immersion following sliding under OCP: (**a**) $Ti_{45}Zr_{45}Nb_5Ta_5$; (**b**) $Ti_{35}Zr_{35}Nb_{25}Ta_5$; (**c**) $Ti_{31.67}Zr_{31.67}Nb_{31.67}Ta_5$.

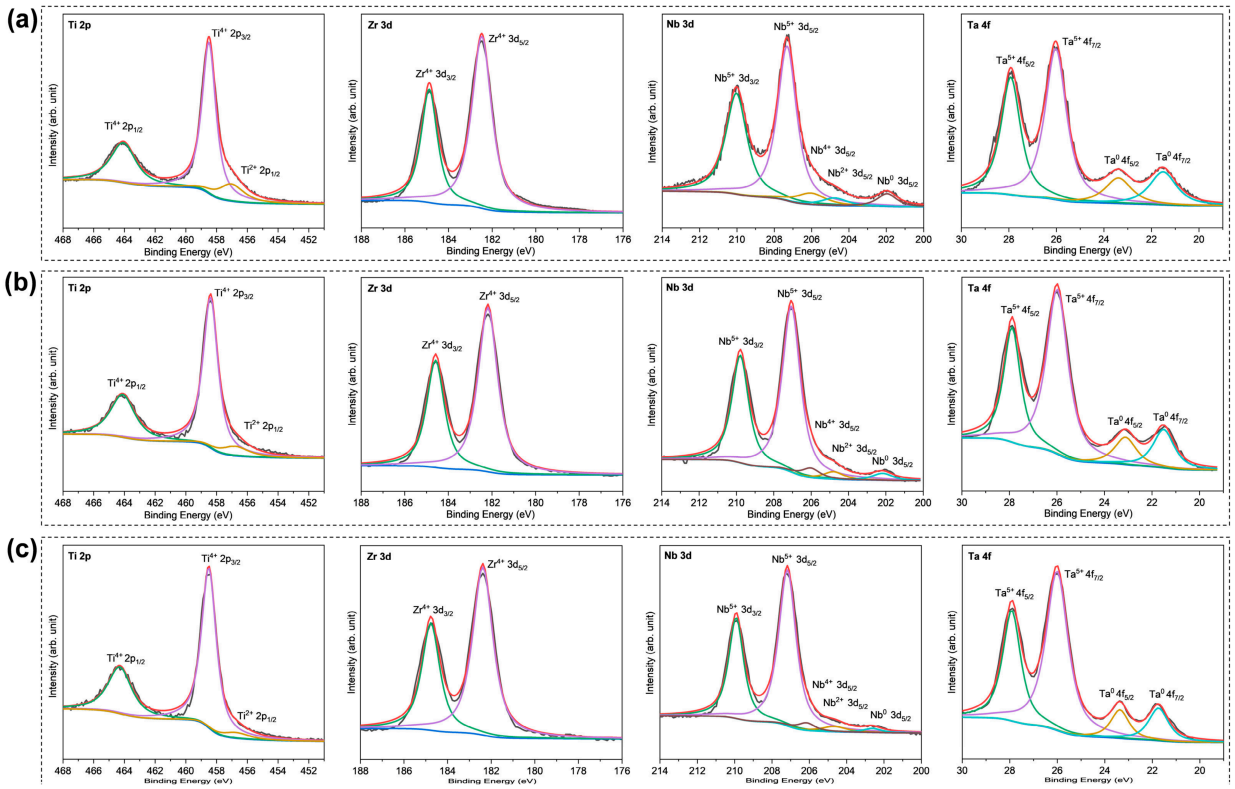

Figure 10. High-resolution XPS spectra (Ti 2p, Zr 3d, Nb 3d and Ta 4f) of the tribocorroded surfaces on TiZrNbTa RMPEAs after 2 h immersion following sliding under OCP: (**a**) $Ti_{45}Zr_{45}Nb_5Ta_5$; (**b**) $Ti_{35}Zr_{35}Nb_{25}Ta_5$; (**c**) $Ti_{31.67}Zr_{31.67}Nb_{31.67}Ta_5$.

As shown in Figure 10, the passive film continuously grows and stabilizes after 2 h of immersion. The intermediate-valence and metallic species of all elements transform into high-valence states. The signals of Ti^0 and Zr^0 completely disappear, and Ti and Zr mainly exist in the forms of Ti^{4+} and Zr^{4+}. By contrast, certain metallic and intermediate-valence species are still detected in the Nb and Ta spectra, indicating that their oxidation and film formation processes remain slower than those of Ti and Zr. As the Nb content in the alloy increases, the relative fraction of high-valence Nb^{5+} oxides in the passive film rises further. These results reveal that the passive film gradually evolves into a mixed oxide film consisting of high-valence oxides of the four elements after long-term immersion, and its compositional evolution is directly related to the elemental ratio of the alloy.

4. Discussion

A substantial increase in the Nb content of the alloy reduces its repassivation rate, which originates from the corresponding decrease in Ti and Zr fractions. Upon exposure of the freshly generated alloy surface to the aqueous solution, the constituent elements dissolve anodically to release metal ions, while hydroxide ions adsorb on the bare metal surface via a partial charge transfer process to form a two-dimensional hydroxide adlayer as the precursor of the passive film, which subsequently precipitates as metal hydroxide and finally dehydrates into the oxide film. The relevant reactions are presented below [51].

$$Me \rightarrow Me^{n+} + ne^- \quad (4)$$

$$Me + OH^- \rightarrow Me - OH_{ads}^{(\gamma-)} + (1-\gamma)e^- \quad (5)$$

$$Me + nOH^- \rightarrow Me(OH)_n + ne^- \quad (6)$$

$$Me^{n+} + nOH^- \rightarrow Me(OH)_n \downarrow \quad (7)$$

$$2Me(OH)_n \rightarrow Me_2O_n + nH_2O \quad (8)$$

In the above reactions, *Me* denotes each constituent metallic element of the alloy (i.e., Ti, Zr, Nb, and Ta). Ti and Zr are passivity-promoting elements, which preferentially adsorb oxygen or hydroxide ions to form oxides after dissolution. According to thermodynamic calculations [52], the equilibrium electrode potentials for the formation of high-valence oxides of each element are listed as follows: Ti → TiO_2 (−1.490 V), Zr → ZrO_2 (−1.887 V), Nb → Nb_2O_5 (−1.015 V), Ta → Ta_2O_5 (−1.166 V). The equilibrium potentials of these redox reactions (vs. the standard hydrogen electrode) reveal that Ti and Zr exhibit more negative values. Thermodynamically, they are more prone to oxidation, preferentially forming stable surface oxide layers and governing the rapid nucleation and growth of oxides. Accordingly, alloys with higher Ti and Zr contents (e.g., $Ti_{45}Zr_{45}Nb_5Ta_5$ alloy) exhibit a faster rise in OCP during passive film growth. The beneficial effect of Nb addition on the stability of passive films has been demonstrated in various Ti-based MPEAs, such as TiZrNb [53], TiZrHfNb [54,55], TiZrNbV [56] and TiVZrNbAl [57]. The underlying mechanism is mainly attributed to the similar ionic radii and electronic configurations of Nb^{5+} and Ti^{4+}. Nb can preferentially dissolve into the TiO_2 oxide and substitute for Ti^{4+}, forming a substitutional defect with an effective positive charge, $Nb_{Ti}^{\cdot}$. According to the Kröger–Vink defect chemistry [58,59], the effective charge of $Nb_{Ti}^{\cdot}$ is compensated by the formation of Ti vacancies ($V_{Ti}^{''''}$), and the two species further associate into electrically neutral defect complexes, thereby reducing the concentration of mobile point defects, such as oxygen vacancies, within the passive film. Therefore, increasing the Nb addition can further reduce the concentration of oxygen vacancy defects in the passive film, thereby suppressing the adsorption of Cl^- and decreasing the inward diffusion rate of cation vacancies generated by the Schottky pair reaction [60], which enables the passive film to maintain its high protective performance and stability.

In tribocorrosion systems, the total measured material loss is not simply the sum of material losses induced by pure electrochemical corrosion and pure wear. For certain alloys, the synergistic effect between wear and corrosion can lead to much more severe material removal than that caused by pure corrosion or pure wear alone [61]. The synergistic effect of tribocorrosion can be quantified using the following equation.

$$W_t = W_f + W_c + \Delta W_s \quad (9)$$

where W_t is the total material loss of the alloy, W_f is the pure mechanical wear component, W_c is the pure corrosion component, and ΔW_s represents the material loss induced by the synergistic effect. In this equation, ΔW_s is the sum of wear-accelerated corrosion (ΔW_{cf}) and corrosion-accelerated wear (ΔW_{fc}). Therefore, ΔW_s is expressed as:

$$\Delta W_s = \Delta W_{fc} + \Delta W_{cf} \quad (10)$$

By measuring the total tribocorrosion volume loss under open-circuit conditions and cathodic potentials, the terms W_t and W_f in Equation (9) can be obtained, respectively. According to Faraday's law, W_c and ΔW_{cf} can be calculated using Equations (11) and (12), respectively [61].

$$W_c = \frac{ItM}{nF\rho} \quad (11)$$

$$\Delta W_{cf} = \frac{I_f tM}{nF\rho} \quad (12)$$

where I is the current under static conditions (A). Under OCP conditions, I_f denotes the difference in corrosion current between static and sliding states. t is the sliding time (s), F is Faraday's constant ($C \cdot mol^{-1}$), ρ is the alloy density ($g \cdot cm^{-3}$), M is the molar mass of the alloy, and n is the number of charges transferred in the oxidation reaction. M is calculated by $\sum x_i M_i$, where x_i is the atomic fraction of each element and M_i is its relative atomic mass. Subsequently, the corrosion-induced wear component (ΔW_{fc}) can be obtained by subtracting ΔW_{cf} from ΔW_s in Equation (10). The individual tribocorrosion components of $Ti_{45}Zr_{45}Nb_5Ta_5$, $Ti_{35}Zr_{35}Nb_{25}Ta_5$ and $Ti_{31.67}Zr_{31.67}Nb_{31.67}Ta_5$ alloys were calculated using the tribocorrosion component decomposition equations, and the results are listed in Table 2. Under open-circuit conditions, the fractions of pure mechanical wear component W_f in the total tribocorrosion loss are 79.11%, 73.23% and 70.72% for $Ti_{45}Zr_{45}Nb_5Ta_5$, $Ti_{35}Zr_{35}Nb_{25}Ta_5$ and $Ti_{31.67}Zr_{31.67}Nb_{31.67}Ta_5$ alloys, respectively, demonstrating that material removal is dominated by pure mechanical friction. Meanwhile, the corresponding fractions of synergistic component ΔW_s are 20.89%, 26.77% and 29.28%. It can be observed from the table that the ΔW_{fc} term is markedly larger than ΔW_{cf} for all tested alloys, indicating that corrosion-accelerated wear dominates the synergistic interaction during tribocorrosion. By contrast, W_c and ΔW_{cf} account for very small proportions of the total material loss. Therefore, mechanical wear governs the material loss of these alloys during tribocorrosion. At -0.8 V_{SCE}, the current density of all alloys stays cathodic during sliding. Friction accelerates the cathodic process and raises cathodic current density (Figure 5), and no anodic peaks appear in the curves, demonstrating that cathodic reactions govern the electrode process and anodic dissolution of newly exposed surfaces is suppressed. Even at OCP, W_c and ΔW_{cf} make up less than 0.2% and 1% of the total loss, respectively (Table 2), and these fractions decline further at -0.8 V_{SCE}. This potential suppresses Cl ion adsorption, resulting in lower Cl content on worn surfaces without observable pitting or corrosion-initiated cracks (Figure 7). Furthermore, many previous studies have used -0.8 V_{SCE} to evaluate pure mechanical wear of Ti-based alloys [62–65]. Accordingly, corrosion contributes negligibly to material loss at this cathodic potential.

Table 2. Calculated tribocorrosion volume components for TiZrNbTa RMPEAs. All components are annual volume losses in mm^3; the multiplicative scaling factor shown in each column header ($\times 10^2$ or $\times 10^{-3}$) must be applied to the tabulated values. The decomposition satisfies $W_t = W_f + W_c + \Delta W_{cf} + \Delta W_{fc}$ for each alloy.

Materials	W_t ($\times 10^2$ mm^3)	W_f ($\times 10^2$ mm^3)	W_c ($\times 10^{-3}$ mm^3)	ΔW_{cf} ($\times 10^2$ mm^3)	ΔW_{fc} ($\times 10^2$ mm^3)
$Ti_{45}Zr_{45}Nb_5Ta_5$	11.244 ± 0.337	8.895 ± 0.267	0.185 ± 0.019	0.096 ± 0.005	2.253 ± 0.068
$Ti_{35}Zr_{35}Nb_{25}Ta_5$	17.313 ± 0.519	12.678 ± 0.380	0.062 ± 0.006	0.152 ± 0.008	4.483 ± 0.134
$Ti_{31.67}Zr_{31.67}Nb_{31.67}Ta_5$	30.809 ± 0.924	21.789 ± 0.654	0.023 ± 0.002	0.289 ± 0.014	8.731 ± 0.262

$Ti_{45}Zr_{45}Nb_5Ta_5$ alloy exhibits a high hardness of 320 ± 10 HV and forms abundant tribofilms on the tribocorroded surface, which are responsible for its low friction coefficient and low tribocorrosion rate. Abrasive wear dominates its wear mechanism, with no evidence of crack propagation or delamination. During friction, fine spalled oxide particles impose mild micro-cutting on the contact surface and induce slight abrasive wear. The tiny wear debris tends to accumulate and agglomerate at the friction interface, and is continuously compressed by the counterbody to form a continuous tribofilm [48,66]. For $Ti_{35}Zr_{35}Nb_{25}Ta_5$ alloy with a hardness of 280 ± 12 HV, the degree of abrasive wear increases. Distinct abrasive wear features can be observed on the tribofilm surface, indicating that tribofilms can mitigate micro-cutting of the alloy substrate by abrasive particles to a certain extent. Nevertheless, the reduced substrate hardness compared with $Ti_{45}Zr_{45}Nb_5Ta_5$

promotes plastic deformation. The locally formed tribofilms cannot accommodate the coordinated deformation of the matrix and thus lose stability. The fractured and spalled tribofilm fragments participate in three-body wear, aggravating abrasive wear and increasing the friction coefficient. Severe ploughing, delamination and plastic deformation occur on the tribocorroded surface of $Ti_{31.67}Zr_{31.67}Nb_{31.67}Ta_5$ alloy, which is related to its low hardness (230 ± 10 HV). Severe surface plastic deformation and ploughing during friction greatly hinder the stable formation of tribofilms, leading to a high friction coefficient and high material loss rate.

Plastic deformation occurs in the near-surface region of materials under frictional shear stress. Dislocation motion and rearrangement during deformation refine grains and induce work hardening in the surface layer [67]. Figure 11 shows the variation in surface hardness of the three alloys after tribocorrosion at different potentials. The degree of work hardening under cathodic potential is markedly higher than that under OCP. During deformation, dislocations accumulate in the shallow subsurface and form pile-ups, resulting in stress concentration and subsequent crack nucleation and propagation. Shallow deformation features can be identified on $Ti_{45}Zr_{45}Nb_5Ta_5$ alloy, while no fatigue cracks are detected (Figure 12a). Its deformed layer remains stable and produces prominent work hardening (Figure 11). Benefiting from higher substrate hardness, $Ti_{35}Zr_{35}Nb_{25}Ta_5$ alloy exhibits milder subsurface deformation than $Ti_{31.67}Zr_{31.67}Nb_{31.67}Ta_5$, which slows the nucleation and propagation of microcracks and leads to slight delamination wear (Figure 12b). Distinct microcrack propagation is observed in the shallow subsurface of the $Ti_{31.67}Zr_{31.67}Nb_{31.67}Ta_5$ alloy (Figure 12c). This weakens the work-hardening effect, and extensive material removal prevents the stable retention of the work-hardened layer.

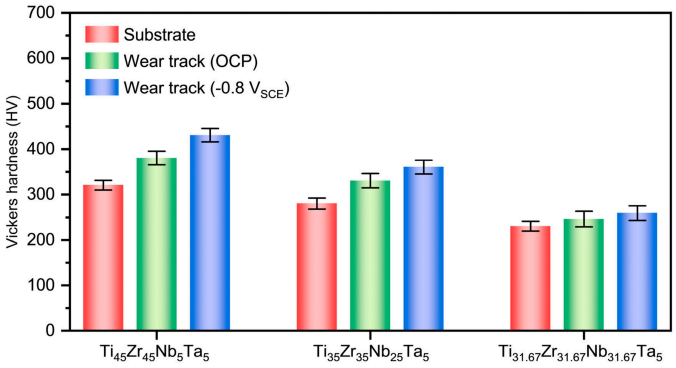

Figure 11. Vickers hardness of the substrate and wear tracks for TiZrNbTa RMPEAs after tribocorrosion under OCP and −0.8 V_{SCE}.

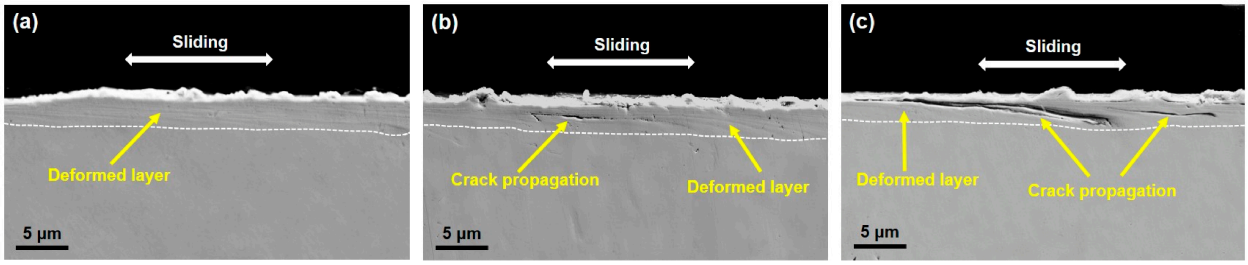

Figure 12. Cross-sectional SEM micrographs showing subsurface deformed layer and crack propagation of wear tracks: (**a**) $Ti_{45}Zr_{45}Nb_5Ta_5$; (**b**) $Ti_{35}Zr_{35}Nb_{25}Ta_5$; (**c**) $Ti_{31.67}Zr_{31.67}Nb_{31.67}Ta_5$.

$Ti_{31.67}Zr_{31.67}Nb_{31.67}Ta_5$ and $Ti_{35}Zr_{35}Nb_{25}Ta_5$ alloys possess dendritic microstructures with obvious intergranular elemental segregation. Such compositional heterogeneity leads to differences in mechanical properties between dendritic and intergranular regions [68]. Under friction, this microstructural inhomogeneity causes incompatible deformation and

triggers local stress concentration for crack initiation. The reduced work hardening under OCP (Figure 11) originates from the synergistic interaction between friction and corrosion [69,70]. Tribocorrosion component calculations reveal that corrosion-accelerated wear accounts for a larger proportion of total material loss for $Ti_{31.67}Zr_{31.67}Nb_{31.67}Ta_5$ alloy. Severe plastic deformation on its surface facilitates microcrack nucleation, and corrosive chloride ions further accelerate crack propagation [49]. Pitting pits generally act as stress concentration sites during plastic deformation, which initiate cracks and promote their further growth [49,71]. As shown in Figure 13, microcrack propagation originating from pitting pits is observed on the tribocorroded surface of $Ti_{31.67}Zr_{31.67}Nb_{31.67}Ta_5$ alloy. EDS analysis demonstrates obvious enrichment of Cl and O elements inside the pits and along crack propagation paths, accompanied by depletion of matrix elements. This phenomenon indicates that chloride attack induces corrosion dissolution within pits and cracks. In summary, increasing Nb content reduces alloy hardness and aggravates elemental segregation. Localized pitting accelerates crack nucleation and propagation during plastic deformation, suppresses the development of work hardening, and consequently intensifies corrosion-accelerated wear.

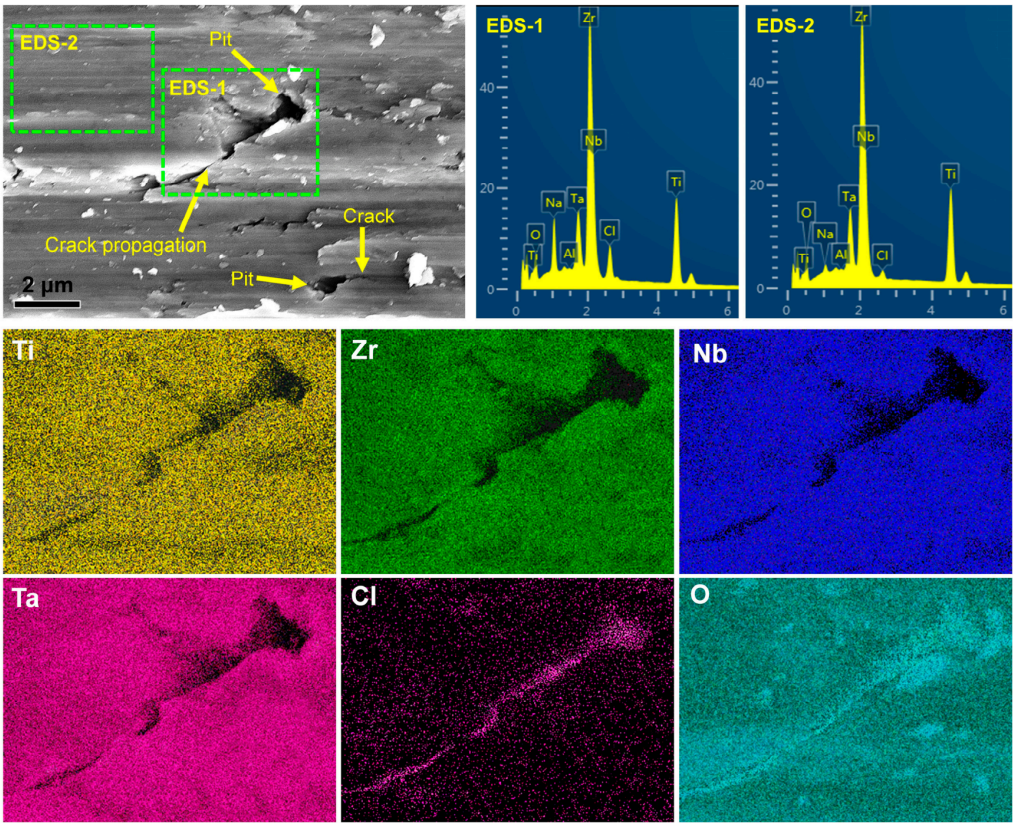

Figure 13. Surface SEM morphology, EDS point spectra and elemental mapping of tribocorroded $Ti_{31.67}Zr_{31.67}Nb_{31.67}Ta_5$ alloy showing pits, cracks and elemental distribution.

This series adopts a design with equal proportional reduction in Ti and Zr and simultaneous increase in Nb content, following a well-established strategy for investigating Nb alloying effects in Ti/Zr-based alloys. Ji et al. [53] employed this same modulation scheme in the biomedical $Ti_{(100-x)/2}Zr_{(100-x)/2}Nb_x$(x = 0–33.33 at.%). Nevertheless, this design carries an inherent limitation: the increase in Nb is accompanied by a concurrent drop in Ti and Zr fractions. Variations in hardness, repassivation and tribocorrosion performance arise from the overall change in the Nb/(Ti + Zr) ratio and cannot be directly attributed to the isolated effect of Nb. Accordingly, this work only establishes performance evolution trends

across different compositions. The role of Nb is indirectly supported by XPS evidence of preferential oxidation and defect chemistry mechanisms. Future designs that fix the total content of Ti and Zr, with Ta serving as a compensating element, will enable quantitative decoupling of the independent contribution of Nb.

5. Conclusions

In this work, three $Ti_{(95-x)/2}Zr_{(95-x)/2}Nb_xTa_5$ (x = 5, 25, 31.67 at.%) RMPEAs with controlled Nb content were fabricated by arc melting, and the effect of Nb content on their microstructure, passive film characteristics and tribocorrosion behavior in NaCl solution was systematically investigated. The main conclusions are as follows:

(1) Three as-cast TiZrNbTa RMPEAs exhibit single-phase BCC solid-solution structures. Increasing Nb content refines grains but intensifies segregation, with Nb and Ta enriched in dendrites and Ti and Zr concentrated in interdendritic regions. The lattice constant decreases, and microhardness declines from 320 ± 10 HV to 230 ± 10 HV.

(2) The i_{corr} and i_{pass} decrease with increasing Nb content, demonstrating that Nb improves the stability of the passive film. Under tribocorrosion conditions, sliding markedly increases the i_{corr} and shifts the E_{corr} negatively. In addition, the resistance of the alloy to friction-induced localized accelerated dissolution is enhanced as Nb content rises.

(3) The repassivation rate of the alloys decreases with increasing Nb content. The rapid nucleation and growth of the passive film on freshly exposed surfaces are dominated by the preferential oxidation of Ti and Zr, while the oxidation of Nb and Ta are relatively sluggish.

(4) As the Nb content increases, the wear mechanism of the alloy changes from mild abrasive wear accompanied by abundant continuous tribofilms to severe ploughing, delamination, plastic deformation and microcrack propagation, and both the friction coefficient and the tribocorrosion rate increase accordingly.

(5) Pure mechanical wear dominates total material loss, while corrosion-accelerated wear is the dominant synergistic component and markedly exceeds wear-accelerated corrosion. This synergistic proportion increases with rising Nb content, indicating that higher Nb alloying enhances the acceleration of wear by corrosion.

(6) Increased Nb content lowers alloy hardness and worsens elemental segregation, readily causing local stress concentration under severe plastic deformation. Localized pits then act as stress raisers, triggering microcrack nucleation, while chloride ions further drive crack propagation, resulting in severe delamination wear. These effects suppress surface work hardening and intensify corrosion-accelerated wear, ultimately degrading the tribocorrosion resistance of TiZrNbTa RMPEAs.

Author Contributions: Methodology, Z.W.; Validation, Z.W.; Formal Analysis, Z.W.; Investigation, Z.W. and J.W.; Resources, Y.Y. and Z.W.; Conceptualization, Z.W.; Data Curation, Z.W., Y.Z. and J.W.; Writing—Original Draft, Z.W.; Writing—Review and Editing, Z.W.; Supervision, Y.Y. and L.Q. All authors have read and agreed to the published version of the manuscript.

Funding: This research was funded by the National Natural Science Foundation of China under Grant No. 52401073 and the Natural Science Foundation of Beijing under Grant No. 2244097.

Data Availability Statement: The original contributions presented in this study are included in the article. Further inquiries can be directed to the corresponding author.

Acknowledgments: We thank Beijing Yijin New Material Technology Co., Ltd. for their support in material preparation, and thank Beijing Yangou Technology Co., Ltd. for their assistance in testing and analysis.

Conflicts of Interest: The authors declare no conflicts of interest.

References

1. Senkov, O.N.; Scott, J.M.; Senkova, S.V.; Miracle, D.B.; Woodward, C. Microstructure and room temperature properties of a high-entropy TaNbHfZrTi alloy. *J. Alloys Compd.* **2011**, *509*, 6043–6048. [CrossRef]
2. Senkov, O.N.; Wilks, G.B.; Miracle, D.B.; Chuang, C.P.; Liaw, P.K. Refractory high-entropy alloys. *Intermetallics* **2010**, *18*, 1758–1765. [CrossRef]
3. Li, Z.; Lai, W.; Wang, B.; Tong, X.; You, D.; Li, W.; Wang, X. A novel $Ti_{42.5}Zr_{42.5}Nb_5Ta_{10}$ multi-principal element alloy with excellent properties for biomedical applications. *Intermetallics* **2022**, *151*, 107731. [CrossRef]
4. Wang, Q.; Kong, X.; Wu, X.; Wu, L.; Yu, Y.; Xin, T.; Qin, J. Effect of the local chemical environment on oxidation resistance mechanisms in AlNbTiZr refractory high entropy alloys: A first-principles study. *Scr. Mater.* **2022**, *213*, 114624. [CrossRef]
5. Adler, T.A.; Walters, R.P. Corrosion and wear of 304 stainless steel using a scratch test. *Corros. Sci.* **1992**, *33*, 1855–1876. [CrossRef]
6. Sun, Y.; Rana, V. Tribocorrosion behaviour of AISI 304 stainless steel in 0.5 M NaCl solution. *Mater. Chem. Phys.* **2011**, *129*, 138–147. [CrossRef]
7. Zirari, T.; Trabadelo, V. A review on wear, corrosion, and wear-corrosion synergy of high entropy alloys. *Heliyon* **2024**, *10*, e25867. [CrossRef] [PubMed]
8. Yang, X.; Li, X. Research on the synergistic damage behavior of tribocorrosion of CoCrFeNi-X (Ti, Mn, Mo, Al) high-entropy alloys. *Tribol. Int.* **2025**, *201*, 110185. [CrossRef]
9. Diao, W.; Wang, J.; Lu, L.; Li, B.; Dai, L.; Cheng, J.; Liao, H.; Wang, X.; Wang, Z.; Xu, Z. Tribocorrosion resistance of high entropy alloy $CoCrFeNiTi_x$ in simulated seawater. *Corros. Sci.* **2026**, *261*, 113595. [CrossRef]
10. Wang, J.; Wen, W.; Cheng, J.; Dai, L.; Li, S.; Zhang, X.; Yang, Y.; Li, H.; Hou, X.; Wu, B.; et al. Tribocorrosion behavior of high-entropy alloys FeCrNiCoM (M = Al, Mo) in artificial seawater. *Corros. Sci.* **2023**, *218*, 111165. [CrossRef]
11. Zhang, X.; Yu, Y.; Li, T.; Wang, L.; Qiao, Z.; Liu, Z.; Liu, W. Effect of the distribution of Cu on the tribo-corrosion mechanisms of $CoCrFeNiCu_{0.3}$ high-entropy alloys. *Tribol. Int.* **2024**, *193*, 109401. [CrossRef]
12. Chen, J.; Zhang, Z.; Hershkovitz, E.; Poplawsky, J.; Dandu, R.S.B.; Hung, C.-Y.; Wang, W.; Yao, Y.; Li, L.; Xin, H. Selective oxidation and nickel enrichment hinders the repassivation kinetics of multi-principal element alloy surfaces. *Acta Mater.* **2024**, *263*, 119490. [CrossRef]
13. Zeng, W.; Li, S.; Ling, Z.; Chen, W.; Yang, X.; Wang, H.; Guo, S.; Fu, Z. Unveiling synergistic tribo-corrosion mechanisms in Ti-rich refractory high-entropy alloys for extreme aluminum processing environments. *Tribol. Int.* **2026**, *214*, 111186. [CrossRef]
14. Ling, Z.; Li, S.; Liu, J.; Chen, W.; Fu, Z. Critical Nb induced interfacial armoring for enhanced molten Al tribo-corrosion resistance in Ti-Nb-Cr refractory alloys. *Wear* **2026**, *584–585*, 206439. [CrossRef]
15. Xiao, J.-K.; Xu, G.-M.; Chen, J.; Rusinov, P.; Zhang, C. Tribocorrosion behavior of TiZrHfNb-based refractory high-entropy alloys. *Wear* **2024**, *536–537*, 205158. [CrossRef]
16. Li, D.; Li, W.; Liu, X. Effect of Nb content on microstructure and mechanical properties of $TiZrVNb_x$ high-entropy energetic alloys. *J. Alloys Compd.* **2025**, *1036*, 181550. [CrossRef]
17. Liu, H.; Zhao, H.; Du, C.; Wang, T.; Jiao, H.; Chen, H.; Gong, X. Effect of different Nb content on microstructure and properties of $AlCrFeNiNb_x$ high entropy alloy. *J. Phys. Conf. Ser.* **2025**, *2954*, 012028. [CrossRef]
18. Dalan, F.C.; Silva Sobrinho, A.S.D.; Nishihora, R.K.; Santos, S.F.; Martins, G.V.; Cardoso, K.R. Effect of Nb and Ti additions on microstructure, hardness and wear properties of AlCoCrFeNi high-entropy alloy. *J. Alloys Compd.* **2025**, *1010*, 177117. [CrossRef]
19. Zhuang, W.; Meng, S.; Xu, T.; Ma, Z.; Jiang, L.; Wang, T.; Cao, Z. Effect of Nb content on microstructure and tribological properties of $AlCrMoNb_xNi$ high-entropy alloy coatings. *Surf. Coat. Technol.* **2025**, *513*, 132477. [CrossRef]
20. Wang, H.; Lin, Z.; Qin, B.; Sun, J.; Su, F.; Liang, Z.; Zhang, Y. High-temperature wear resistance improvement mechanism of $TiAlCrNiSiNb_x$ high-entropy alloy films through sliding wear-induced gradient nanostructure. *Tribol. Int.* **2024**, *196*, 109725. [CrossRef]
21. Meyer, Y.A.; Bonatti, R.S.; Bortolozo, A.D.; Osório, W.R. Electrochemical behavior and compressive strength of Al-Cu/xCu composites in NaCl solution. *J. Solid State Electrochem.* **2021**, *25*, 1303–1317. Correction in *J. Solid State Electrochem.* **2021**, *25*, 2455. https://doi.org/10.1007/s10008-021-05006-9. [CrossRef]
22. McCafferty, E. Validation of corrosion rates measured by the Tafel extrapolation method. *Corros. Sci.* **2005**, *47*, 3202–3215. [CrossRef]
23. Wang, Z.; Yan, Y.; Su, Y.; Qiao, L. Effects of stirring action during friction on electrode processes of AISI 304 stainless steel in sulphuric acid. *Electrochim. Acta* **2019**, *298*, 756–769. [CrossRef]
24. Nguyen, V.T.; Qian, M.; Shi, Z.; Song, T.; Huang, L.; Zou, J. A novel quaternary equiatomic Ti-Zr-Nb-Ta medium entropy alloy (MEA). *Intermetallics* **2018**, *101*, 39–43. [CrossRef]
25. Yang, W.; Pang, S.; Liu, Y.; Wang, Q.; Liaw, P.K.; Zhang, T. Design and properties of novel Ti–Zr–Hf–Nb–Ta high-entropy alloys for biomedical applications. *Intermetallics* **2022**, *141*, 107421. [CrossRef]
26. Weng, W.; Biesiekierski, A.; Lin, J.; Ozan, S.; Li, Y.; Wen, C. Development of beta-type Ti-Nb-Zr-Mo alloys for orthopedic applications. *Appl. Mater. Today* **2021**, *22*, 100968. [CrossRef]

27. Nagase, T.; Mizuuchi, K.; Nakano, T. Solidification microstructures of the ingots obtained by arc melting and cold crucible levitation melting in TiNbTaZr medium-entropy alloy and TiNbTaZrX (X = V, Mo, W) high-entropy alloys. *Entropy* **2019**, *21*, 483. [CrossRef] [PubMed]
28. Aranda, V.A.; Figueroa, I.; Amigó, V.; Gonzalez-Ojeda, R.; Lozada, O.; Vidilli, A.L.; Otani, L.; González, G. Effect of Mo on high entropy Ti-Nb-Zr-Ta alloy: Phase equilibria, microstructure and mechanical properties. *J. Alloys Compd.* **2023**, *960*, 170758. [CrossRef]
29. Nguyen, V.; Qian, M.; Shi, Z.; Song, T.; Huang, L.; Zou, J. Compositional design of strong and ductile (tensile) Ti-Zr-Nb-Ta medium entropy alloys (MEAs) using the atomic mismatch approach. *Mater. Sci. Eng. A* **2019**, *742*, 762–772. [CrossRef]
30. Vasilescu, C.; Drob, S.; Moreno, J.C.; Osiceanu, P.; Popa, M.; Vasilescu, E.; Marcu, M.; Drob, P. Long-term corrosion resistance of new Ti–Ta–Zr alloy in simulated physiological fluids by electrochemical and surface analysis methods. *Corros. Sci.* **2015**, *93*, 310–323. [CrossRef]
31. Heakal, F.E.-T.; Awad, K.A. Electrochemical corrosion and passivation behavior of titanium and its Ti-6Al-4V alloy in low and highly concentrated HBr solutions. *Int. J. Electrochem. Sci.* **2011**, *6*, 6483–6502. [CrossRef]
32. Soriano Carranza, A.G.; Sánchez, L.A.; Roncagliolo, P.; Espinoza Vázquez, A.; Ramos, C.; Lara, G.A.; González, G.; Rodríguez Gómez, F.J.; Figueroa, I.A. Effect of Ti Content on Passive Film Formation and Growth Kinetics in $Ni_{50}Nb_{50-x}Ti_x$ Metallic Glasses. *Metals* **2026**, *16*, 768. [CrossRef]
33. Ding, Z.; Yuan, Q.; Wang, H.; Tang, Y.; Tan, Y.; He, Q. Anticorrosion behaviour and tribological properties of AZ31 magnesium alloy coated with Nb_2O_5/Nb_2O_5–Mg/Mg layer by magnetron sputtering. *RSC Adv.* **2022**, *12*, 28196–28206. [CrossRef] [PubMed]
34. Yu, S.; Scully, J. Corrosion and passivity of Ti-13% Nb-13% Zr in comparison to other biomedical implant alloys. *Corrosion* **1997**, *53*, 965–976. [CrossRef]
35. Boddy, P.; Kahng, D.; Chen, Y. Oxygen evolution on potassium tantalate anodes. *Electrochim. Acta* **1968**, *13*, 1311–1328. [CrossRef]
36. Wang, L.; Yu, H.; Wang, S.; Chen, B.; Wang, Y.; Fan, W.; Sun, D. Quantitative analysis of local fine structure on diffusion of point defects in passive film on Ti. *Electrochim. Acta* **2019**, *314*, 161–172. [CrossRef]
37. Trasatti, S. Electrocatalysis in the anodic evolution of oxygen and chlorine. *Electrochim. Acta* **1984**, *29*, 1503–1512. [CrossRef]
38. Trasatti, S. Progress in the understanding of the mechanism of chlorine evolution at oxide electrodes. *Electrochim. Acta* **1987**, *32*, 369–382. [CrossRef]
39. Karlsson, R.K.; Cornell, A. Selectivity between oxygen and chlorine evolution in the chlor-alkali and chlorate processes. *Chem. Rev.* **2016**, *116*, 2982–3028. [CrossRef] [PubMed]
40. Karlsson, R.K.; Hansen, H.A.; Bligaard, T.; Cornell, A.; Pettersson, L.G. Ti atoms in $Ru_{0.3}Ti_{0.7}O_2$ mixed oxides form active and selective sites for electrochemical chlorine evolution. *Electrochim. Acta* **2014**, *146*, 733–740. [CrossRef]
41. Milošev, I. The effect of biomolecules on the behaviour of CoCrMo alloy in various simulated physiological solutions. *Electrochim. Acta* **2012**, *78*, 259–273. [CrossRef]
42. Dyer, C.; Leach, J. Breakdown and efficiency of anodic oxide growth on titanium. *J. Electrochem. Soc.* **1978**, *125*, 1032–1038. [CrossRef]
43. Frankel, G. Pitting corrosion of metals: A review of the critical factors. *J. Electrochem. Soc.* **1998**, *145*, 2186–2198. Correction in *J. Electrochem. Soc.* **1998**, *145*, 2970a. https://doi.org/10.1149/1.1838748. [CrossRef]
44. Mischler, S.; Debaud, S.; Landolt, D. Wear-Accelerated Corrosion of Passive Metals in Tribocorrosion Systems. *J. Electrochem. Soc.* **1998**, *145*, 750–759. [CrossRef]
45. Diomidis, N.; Mischler, S.; More, N.S.; Roy, M.; Paul, S.N. Fretting-corrosion behavior of β titanium alloys in simulated synovial fluid. *Wear* **2011**, *271*, 1093–1102. [CrossRef]
46. Vieira, A.C.; Rocha, L.A.; Papageorgiou, N.; Mischler, S. Mechanical and electrochemical deterioration mechanisms in the tribocorrosion of Al alloys in NaCl and in $NaNO_3$ solutions. *Corros. Sci.* **2012**, *54*, 26–35. [CrossRef]
47. Ureña, J.; Tsipas, S.; Pinto, A.M.; Toptan, F.; Gordo, E.; Jiménez-Morales, A. Corrosion and tribocorrosion behaviour of β-type Ti-Nb and Ti-Mo surfaces designed by diffusion treatments for biomedical applications. *Corros. Sci.* **2018**, *140*, 51–60. [CrossRef]
48. Bhardwaj, V.; Zhou, Q.; Zhang, F.; Han, W.; Du, Y.; Hua, K.; Wang, H. Effect of Al addition on the microstructure, mechanical and wear properties of TiZrNbHf refractory high entropy alloys. *Tribol. Int.* **2021**, *160*, 107031. [CrossRef]
49. Cao, S.; Mischler, S. Modeling tribocorrosion of passive metals—A review. *Curr. Opin. Solid State Mater. Sci.* **2018**, *22*, 127–141. [CrossRef]
50. Archard, J.F. Contact and Rubbing of Flat Surfaces. *J. Appl. Phys.* **1953**, *24*, 981–988. [CrossRef]
51. Ai, Z.; Jiang, J.; Sun, W.; Jiang, X.; Yu, B.; Wang, K.; Zhang, Z.; Song, D.; Ma, H.; Zhang, J. Enhanced passivation of alloy corrosion-resistant steel $Cr_{10}Mo_1$ under carbonation—Passive film formation, the kinetics and mechanism analysis. *Cem. Concr. Compos.* **2018**, *92*, 178–187. [CrossRef]
52. Pourbaix, M. *Atlas of Electrochemical Equilibria in Aqueous Solutions*; National Association of Corrosion Engineers: Houston, TX, USA, 1974. [CrossRef] [PubMed]

53. Ji, P.; Li, B.; Chen, B.; Wang, F.; Ma, W.; Zhang, X.; Ma, M.; Liu, R. Effect of Nb addition on the stability and biological corrosion resistance of Ti-Zr alloy passivation films. *Corros. Sci.* **2020**, *170*, 108696. [CrossRef]
54. Tanji, A.; Fan, X.; Sakidja, R.; Liaw, P.K.; Hermawan, H. Niobium addition improves the corrosion resistance of $TiHfZrNb_x$ high-entropy alloys in Hanks' solution. *Electrochim. Acta* **2022**, *424*, 140651. [CrossRef]
55. Tanji, A.; Fan, X.; Sakidja, R.; Liaw, P.K.; Hermawan, H. Role of Niobium on the Passivation Mechanisms of TiHfZrNb High-Entropy Alloys in Hanks' Simulated Body Fluid. *J. Funct. Biomater.* **2024**, *15*, 305. [CrossRef] [PubMed]
56. Wang, D.; Zhang, S.; Cui, J.; Zeng, S.; Zou, Y.; Liu, J.; Han, D.; Liu, C.; Chen, X.-Q.; Ma, H.; et al. Ultra-high pitting resistance in high-entropy alloys by simultaneous enhancement of complex oxide stability and bond energy. *J. Mater. Sci. Technol.* **2027**, *279*, 154–164. [CrossRef]
57. Li, X.; Yuan, J.; Lu, K.; Chong, K.; Liu, L.; Zhang, Z.; Chen, Y.; Xu, S.; Jiang, B.; Liang, X. Corrosion resistance and passive film stability of laser direct energy deposited TiVZrNbAl lightweight multi-principal element alloy. *Corros. Sci.* **2024**, *239*, 112391. [CrossRef]
58. Alvar, E.N.; Zhou, B.; Eichhorn, S.H. Carbon-embedded mesoporous Nb-doped TiO_2 nanofibers as catalyst support for the oxygen reduction reaction in PEM fuel cells. *J. Mater. Chem. A* **2016**, *4*, 6540–6552. [CrossRef]
59. Li, W.; Bak, T.; Atanacio, A.; Nowotny, J. Photocatalytic properties of TiO_2: Effect of niobium and oxygen activity on partial water oxidation. *Appl. Catal. B Environ.* **2016**, *198*, 243–253. [CrossRef]
60. Wang, Q.; Zhang, B.; Ren, Y.; Yang, K. A self-healing stainless steel: Role of nitrogen in eliminating detrimental effect of cold working on pitting corrosion resistance. *Corros. Sci.* **2018**, *145*, 55–66. [CrossRef]
61. Landolt, D.; Mischler, S.; Stemp, M. Electrochemical methods in tribocorrosion: A critical appraisal. *Electrochim. Acta* **2001**, *46*, 3913–3929. [CrossRef]
62. Xu, W.; Du, Z.; Wang, Z.; Ran, X.; Li, Z.; Chen, R.; Zhu, X.; Zhang, X.; Zhang, J.; Lu, X. A comparative study on the corrosion, wear, and tribocorrosion performances of Ti-6.5 Al–2Zr–1Mo–1V (TA15) alloy fabricated by selective laser melting and laser metal deposition. *J. Mater. Res. Technol.* **2024**, *30*, 6245–6253. [CrossRef]
63. Lu, X.; Zhang, D.; Xu, W.; Yu, A.; Zhang, J.; Tamaddon, M.; Zhang, J.; Qu, X.; Liu, C.; Su, B. The effect of Cu content on corrosion, wear and tribocorrosion resistance of Ti-Mo-Cu alloy for load-bearing bone implants. *Corros. Sci.* **2020**, *177*, 109007. [CrossRef]
64. Min, J.; Wang, X.-Z.; Wang, Y.; Bai, Y.; Sabola, S.A.; Gong, W.; Wang, L.; Li, J.; Li, Z. Tribocorrosion in nitric acid of Zr alloy, Ti alloy, and 310 SS used for reprocessing of spent nuclear fuel. *Tribol. Int.* **2025**, *201*, 110184. [CrossRef]
65. Wang, L.; Xie, Y.-F.; Lu, X.; Wang, F. Tribocorrosion behavior of plasma electrolytic oxidation coatings on TC4 alloy. *Corros. Sci.* **2026**, *268*, 113918. [CrossRef]
66. Hiratsuka, K.I.; Muramoto, K.I. Role of wear particles in severe–mild wear transition. *Wear* **2005**, *259*, 467–476. [CrossRef]
67. Zhang, Y.; Wei, Q.; Niu, H.; Li, Y.; Chen, C.; Yu, Z.; Bai, X.; Zhang, P. Formation of nanocrystalline structure in tantalum by sliding friction treatment. *Int. J. Refract. Met. Hard Mater.* **2014**, *45*, 71–75. [CrossRef]
68. Wang, S.-P.; Xu, J. TiZrNbTaMo high-entropy alloy designed for orthopedic implants: As-cast microstructure and mechanical properties. *Mater. Sci. Eng. C* **2017**, *73*, 80–89. [CrossRef] [PubMed]
69. Yazdi, R.; Ghasemi, H.; Abedini, M.; Wang, C.; Neville, A. Tribocorrosion behaviour of Ti_6Al_4V under various normal loads in phosphate buffered saline solution. *Trans. Nonferrous Met. Soc. China* **2020**, *30*, 1300–1314. [CrossRef]
70. Zhang, Y.; Yin, X.; Wang, J.; Yan, F. Influence of microstructure evolution on tribocorrosion of 304SS in artificial seawater. *Corros. Sci.* **2014**, *88*, 423–433. [CrossRef]
71. Sun, Y.; Haruman, E. Tribocorrosion behaviour of low temperature plasma carburised 316L stainless steel in 0.5 M NaCl solution. *Corros. Sci.* **2011**, *53*, 4131–4140. [CrossRef]

Disclaimer/Publisher's Note: The statements, opinions and data contained in all publications are solely those of the individual author(s) and contributor(s) and not of MDPI and/or the editor(s). MDPI and/or the editor(s) disclaim responsibility for any injury to people or property resulting from any ideas, methods, instructions or products referred to in the content.